RAM

ROBOTICS AND MECHATRONICS

Design and Prototyping of McRobot Version 3.1: Multi-modality Compatible Robot for Image Guided Minimally Invasive Intervention and Therapy

X. (Xiaolong) Zhi

MSc Report

UNIVERSITY OF TWENTE.

MIRA **CTIT**
BIOMEDICAL TECHNOLOGY
AND TECHNICAL MEDICINE

Abstract

Magnetic resonance imaging (MRI) compatible robotics is one of the new technologies for performing image guided minimally invasive interventions (MII) such as cancer biopsy gathering or brachytherapy. In this report, design, prototype, and test of a patient-mounted image-guided surgical robotic system for MII are reported.

The technical requirements of the robot are determined based on a literate study regarding to different related products and experiences around the world. The robot consists of four degrees of freedom (DoF), making it able to orientate, insert, and rotate an axisymmetric surgical tool, such as a needle. With the patient-mounted method the robot compensates the patient's motion passively and reduces three translation DoFs. To actuate the robot, an MRI compatible back-drivable pneumatic step actuator is designed. The requirements of the actuator are determined based on a kinematic model of the robot. The actuator and remaining components of the robot are 3D printed and laser-cut out of MRI compatible materials. To actuate the robot efficiently, five actuators are installed.

Tests indicate that the actuator achieves a step motion of approximately 12°. With a lab-made DC motor based pneumatic distributor, a speed of approximately 1.25rad/s can be achieved. With the air pressure of 5bar, an output torque of approximately 125Nmm can be achieved. The speed can be increased by replacing the lab-made DC motor based pneumatic distributor with commercial valve terminal with higher frequency. The output torque can be increased by increasing the air pressure. The robot is able to penetrate its tool into a silicone gel based soft phantom. The insertion accuracy is roughly measured to be 2mm. With the lab-made DC motor based pneumatic distributor, a maximum insertion speed of the tool is roughly measured to be 11.6mm/s. Tests inside an MRI scanner indicate that the robot, including the actuator, is fully MRI compatible.

Glossary

Abbreviation	Full meaning
MIS	Minimally invasive surgery
OS	Open surgery
CT	Computed tomography
MRI	Magnetic resonance imaging
MII	Minimally invasive intervention
McRobot	MRI compatible robot
DoF	Degree of freedom
CE	Conformité Européene
RaM	Robotics and Mechatronics
FEM	Finite element modelling

List of Figures

List of Tables

List of Tables

Contents

1. Introduction

Cancer had been one of the leading causes of death worldwide.[1][2] New technologies for solving cancer related problems have been developed, among them minimally invasive surgery (MIS), image-guided interventions and robotics are three very promising advancements. The combination of these three developments is therefore an attractive strategy towards achieving better results for patients, practitioners and medical industry. In this project, an image-guided surgical robotic system for minimally invasive intervention is designed and prototyped. In this chapter motivations and objectives of this project are introduced.

1.1 Motivation

Compared to conventional open surgery (OS), MIS has many advantages. For example, MIS does not require large incision on patients, therefore resulting in a quicker recovery time, shorter stay at the hospital and a lower risk of infection.[3]

In MIS, in order to guide a tool to the desired location, visual feedback is required. A possible method is to use non-invasive imagers, in which, ultrasound and computed tomography (CT) are two widely used conventional modalities to guide the minimally invasive interventional surgery. Compared to these conventional modalities, magnetic resonance imaging (MRI) provides several benefits that make it attractive for guiding interventions. Firstly, MRI offers a plethora of soft-tissue contrast mechanisms that allow the assessment of both anatomical morphology and function. Secondly, MRI is an intrinsically 3D modality that allows unrestricted selection of oblique 3D or multi-plane imaging. Thirdly, in contrast to other radiological imaging systems which include high exposure to radioactive radiations, MRI is safe for patients and medical staff as it does not use ionizing radiation.[4]

Robotics is also one of the promising developments towards diagnosis and treatment cancer. Robotics can compensate natural tremors and enhance the operation force, therefore offering higher accuracy and efficiency than manual operations, as well as high level of steadiness. With robotics, operators can stay far away from the patient, therefore avoiding exposure and infection risk.

The combination of MIS, image-guided interventions and robotics, the MRI compatible assistant robot for minimally invasive intervention (MII), is believed to be the future of cancer diagnosis and treatment and many groups around the world have focused on the design of the robots for MRI compatible minimally invasive intervention in last decades. Few clinical available products, however, have been reported due to various difficulties. Ferromagnetic materials which are applied in conventional robotic and mechatronic systems are not suitable in the MRI environment. Lack of MRI compatible actuators and sensors is another problem hindering the development of MRI compatible robotics. What is more, many current designs are technology driven while the workflow of the clinical operation is not fully taken into account.

1.2 Thesis Objectives

The main objective of this project is to make a **M**RI **c**ompatible **Robot** (McRobot) suitable for closed bore MRI for minimally invasive intervention with axisymmetric tools. The region of human body that the robot operates is concentrated on the chest and abdomen. Human motions compensation, MRI compatibility, and adaption with the compact area between the patient's chest and scanner bore are the three key challenges in this project.

1.3 Thesis Organization

The state of art regarding to current achievements on MRI compatible robot is represented in Chapter 2 categorized in MRI compatible robots, actuators, materials and sensors. In Chapter 3, the functional requirements of McRobot, as well as that of the actuator are prior determined. Then the actuator and robot are designed based on the requirements. The test of the prototype and the result are represented in Chapter 4. The conclusions and possible future works are discussed in Chapter 5.

2. State of Art

The benefits of MRI compatible surgery robot are encouraging extensive research by different institutes around worlds, although few of them has developed commercial product successfully.

In this chapter it firstly represents an overview of designs for image-guided minimally invasive intervention robots around the world, concentrating on the abdomen and chest, including some products that are not MRI compatible but still referable regarding their kinematic structure design. Secondly, as the actuator design is an important part in this project, a literature research focusing on MRI compatible actuators is therefore represented. Thirdly, the limitations of materials introduced by MRI environment are analysed. The MRI compatible sensors is not included in this assignment, a short literature research is still represented such that a completed state of art is given.

2.1 Image-Guided Minimally Interventional Robots

The determination of degrees of freedom (DoF) of the image-guided intervention robots depends on the requirements for the performance, complexity and required dexterity of an intervention as well as the restrictions composed by the imaging device. Several groups worldwide have developed image-guided MIS robots concentrating on the abdomen and chest, demonstrating the feasibility of different kinematic designs.

A MRI compatible robotic system for biopsy and therapy of liver tumours was demonstrated by Hata et al.[5] as shown in Figure 2.1. It contains three translational DoFs for the needle positioning actuated by ultrasonic (piezoelectric) motors and two passive DoFs for the needle orientation and insertion. With the combination of active and passive DoFs, surgeons can freely select the insertion path of the needle while pointing at the pre-defined point. As opposed to many groups that placing the robot over the patient or surgeon's head, this robot is put under the side of the patient couch.
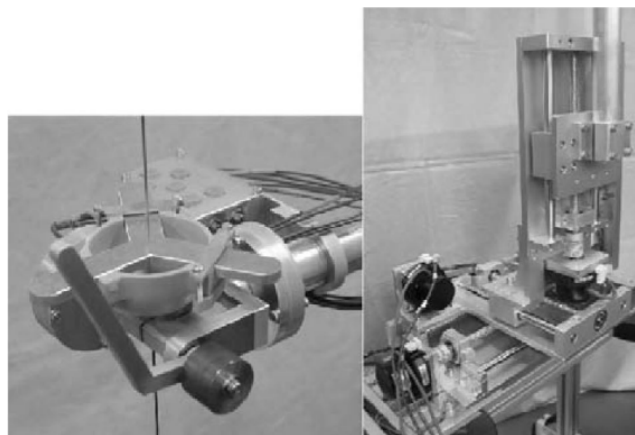
Figure 2. 1 MR compatible RCM needle guiding robot by Nobuhiko Hata et al. Left: Passive two DoFs end effector. Right: Active three DoFs XYZ stage.[5]

An MRI compatible robotic system for biopsy and therapy of breast cancer was demonstrated by Tsekos et al.[6] and was improved further by Larson et al.[7] as shown in Figure 2.2. This device has five DoFs: rotation around the vertical axis, compression of the moving plate, linear motion of the needle guide along the vertical axis, angulation of the needle guide, and depth of the needle insertion. In the original prototype, the first four motions are actuated with ultrasonic piezoelectric motors and the insertion is actuated with a manually activated mechanical link. In the improved prototype, the depth of insertion is actuated by a screw driver driven by an ultrasonic motor via a flexible shaft.
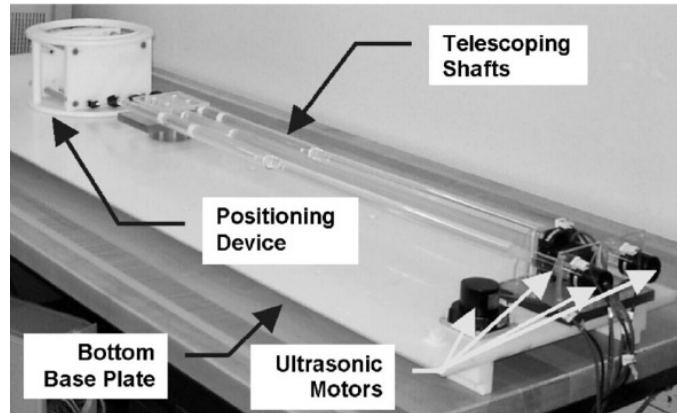
Figure 2. 2 Overview photograph of the device developed by Blake Larson et al. (patient couch not shown).[7]

Another MRI compatible interventional system for general purpose was developed and improved by Tsekos et al.[8][9] as shown in Figure 2.3. This device consists of seven DoFs: A Cartesian positioner provides three translational DoFs for the global positioning of the arm. The arm has three rotational DoFs and a translational DoF to adjust the depth of the needle insertion. The third rotational DoFs is redundant but is deemed necessary as this maintains the main linkage of the arm away from the patient while setting the orientation of the needle. The depth of the insertion is actuated manually and other six DoFs are actuated automatically. This device is developed mainly for the minimally invasive surgery in the abdominal and thoracic cavities.
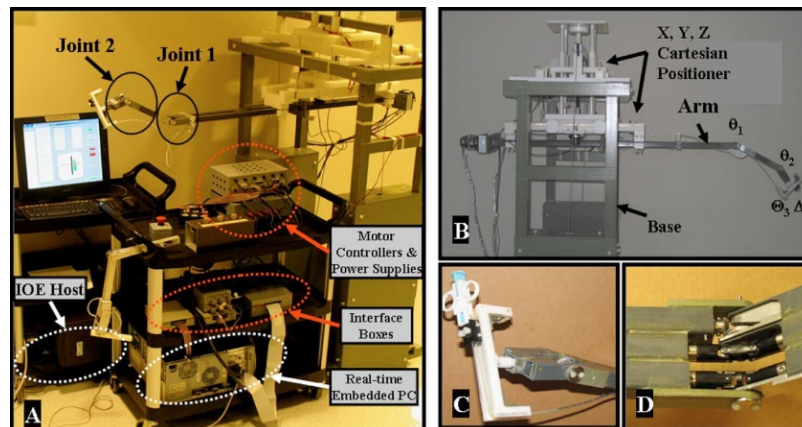
Figure 2. 3 Photographs of the system by Nikolaos Tsekos et al. A. The major hardware components. B. Side view photograph of the manipulator with the arm and the XYZ positioner anchored on the base. C. Close-up of the end-effector with a biopsy needle attached on it. D. Close-up of the first elbow.[8]

Bricault et al.[10] developed a light puncture robotic system mounted to the patient to perform interventions as shown in Figure 2.4. This system possesses five DoFs and is composed of two parts. The main part is the needle-holder that is directly laid above the patient. This part provides a translational DoFs and two rotational DoFs. The other part of this system is composed of a support frame and four actuators providing two translational DoFs. In this system, there are some highlights which worth being referenced in the McRobot design: Firstly, actuators can be disengaged to perform a manual prepositioning of the needle-holder. Secondly, the needle-holder part includes clumps to grasp the needle. Thirdly, a fast linear pneumatic actuator to perform a fast puncture in a linear motion is applied.
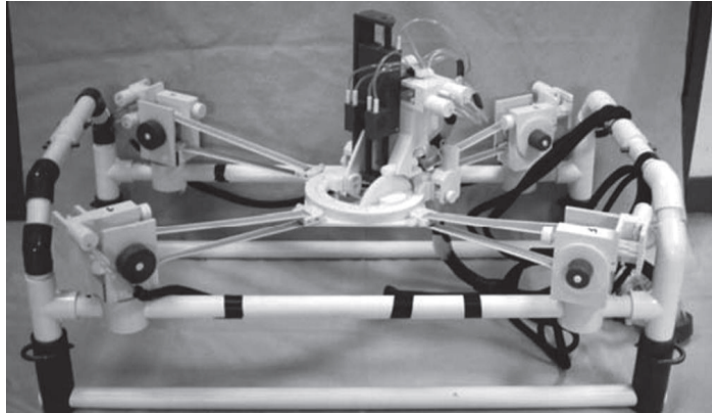
Figure 2. 4 The entire light puncture robot developed by Ivan Bricault et al.[10]

A patient-mounted device for CT guided percutaneous interventions driven by four DoFs was developed by Walsh et al.[11] as shown in Figure 2.5, which is not MRI compatible. A spherical mechanism is introduced to provide two rotational DoFs of the needle through a pair of concentric hoops. The axes of these two hoops are coplanar and their intersection point is on the mechanical pivot of the needle. Such a center of motion on the location of the incision on the patient's skin helps to avoid unexpected lateral motion in case of system malfunction and eases the control of the robot. The carriage riding in the two hoops provides another two DoFs: the insertion of the needle and a grab/release mechanism. Although it is not a MRI compatible device, its kinematic configuration can still be referred, especially its solution of the passive compensation of human motion.
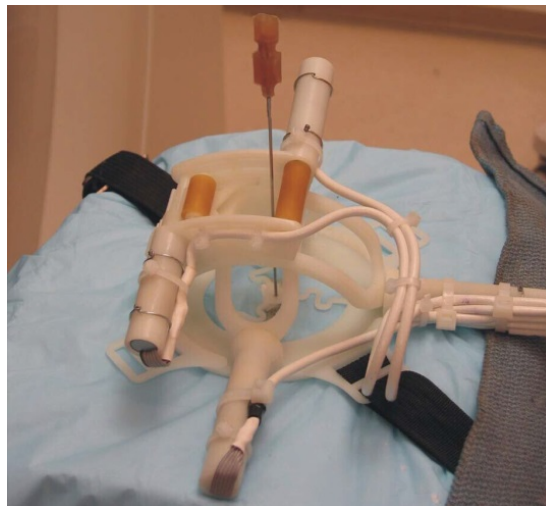
Figure 2. 5 Beta prototype by Conor J. Walsh et al. The disposable actuator is shown strapped to a thoracic phantom. The needle is not gripped by the device and is free to move.[11]

Benjamin Maurin et al.[12] presented another CT guided patient-mounted robotic platform which is consisted of a parallel structure made of a six-bar linkage associated to a four-bar linkage through a common platform, as shown in Figure 2.6. It contains five DoFs, including three DoFs for positioning and two for the orientation. In which, three DoFs are imposed by three actuators of the six-bar linkage. The four-bar linkage constrains the remaining DoFs of the six-bar linkage through two other actuators. The whole system consequently results in a 2R3T parallel manipulator driven by five actuators.

5

Figure 2. 6 CT-Bot prototype by Benjamin Maurin et al. with a passive needle guide.[12]

A couple of MRI compatible robots have received Conformité Européene (CE) mark for image-guided percutaneous interventions. One of them, which is currently in clinical use is the InnoMotion developed by Melzer et al.[13][14] as shown in Figure 2.7. This system is developed for various tasks in spine, liver, kidney, breast etc. Its arm is consisted of five DoFs actuated pneumatically, in which, three of them are translational and two are rotational. The arm is attached to an orbiting ring that is mounted to the patient table and can be manually prepositioned.

Figure 2. 7 InnoMotion robotic assistance system on the patient table of a clinical 1.5T whole body MR system.[14]

A summary of the robotic systems mentioned above, concentrating on their kinematic structures, is presented in Table 2.1.

Table 2. 1 Summary of the MRI compatible robotic systems reviewed.

| Product | Author | Application | Number of DoFs | | Atonomy |
			Translational	Rotational	
	Nobuhiko Hata et al.[5]	Liver tumors intervention	3	2	Three active translational DoFs and two passive rotational DoFs
	Blake Larson et al.[7]	Breast biopsy	3	2	All DoFs active
	Nikolaos Tsekos et al.[8]	General purpose	4	3	All DoFs active except manual insertion
	Ivan Bricault et al.[10]	General purpose	3	2	All DoFs active while actuators can be disengaged for manual prepositioning
	Conor J. Walsh et al.[11]	General purpose	1	3	All DoFs active
	Benjamin Maurin et al.[12]	General purpose	3	2	All DoFs active except manual insertion
	Andreas Melzer et al.[13][14]	General purpose	3	3	Active: two rotational DoFs and three translational DoFs Manual: one rotational DoF and one Translational DoF
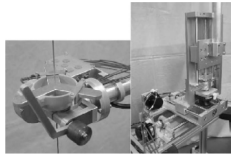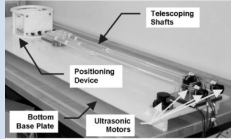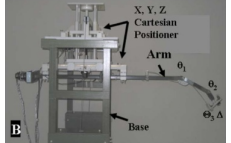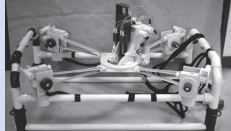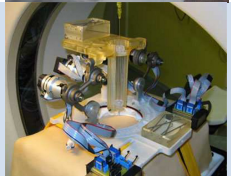
2.2 MRI Compatible Actuators

In order to actuate the robot, MRI compatible actuators or power transmission systems are required. Traditional electromagnetic actuators, piezoelectric actuators, and pneumatic actuators are three main strategies for actuation methods to actuate MRI compatible robots. However, neither electromagnetic actuators nor piezoelectric actuators can operate inside

the scanner. In the McRobot project, pneumatic actuator is preferred. In this section, several pneumatic actuators designed by groups around the world are compared.

A pneumatic nutation motor was developed by Suzumori et al.[15] This motor contains a pair of bevel gears: a cone-shaped bevel gear as nutator and cup-shaped bevel gear as rotor. Three pneumatic cylinders are connected to the nutator allowing applying pressure to the cylinder. When the pressure is applied to the cylinder sequentially, the nutation of the nutator caused by the linear motion of the cylinders is converted into rotation of the rotor. The working principle and prototype are shown in Figure 2.8.
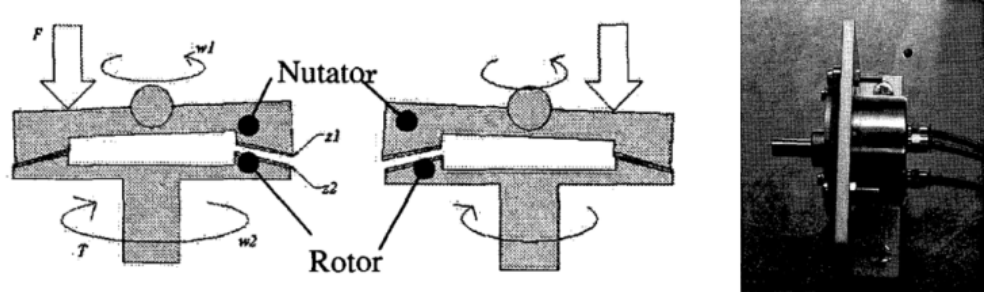
Figure 2. 8 Left: Driving principle of nutation motor by Koichi Suzumori et al. Right: Developed nutation motor.[15]

Another pneumatic stepping actuator applying a similar driving principle was developed by Sajima et al.[16] The rotation is achieved by two kinds of gears, which are one rotation gear and three direct acting gears. In which, each direct gear is connected to a cylinder. The concept configuration and overview of the prototype are shown in Figure 2.9. The three direct acting gears are pushed by the pistons in the pneumatic cylinders sequentially, resulting in the rotation gear rotates and engages with the corresponding direct acting gear. The direction of rotation can be switched by changing the sequence of direct acting gears.
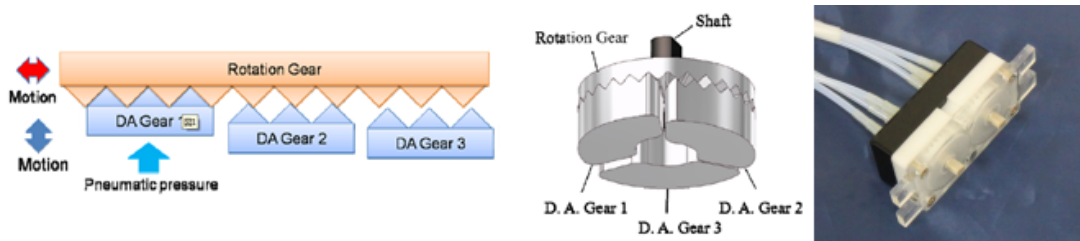
Figure 2. 9 Left: 2D schematic representation of the motor by Hiroyuki Sajima et al. Middle: Main components of the step actuation. Right: Overview of the prototype.[16]

A more complex pneumatic step actuator called PneuStep was developed by Stoianovici et al.[17][18] Its kinematic diagram and prototype are shown in Figure 2.10. The step motion is achieved by pressurizing the cylinders (D1-D3) sequentially, similarly as the previous two designs.

Figure 2. 10 Left: Kinematic diagram of Pneustep motor by Dan Stoianovici et al. Right: Two sizes of the motor prototypes.[17][18]

A pneumatic step motor with different driving structure was developed by Chen et al.[19] The assembly design of the pneumatic step motor consisting of six key components is shown

in Figure 2.11. The driving force of the mechanism is provided by two cylinders that coupled along a rotation axis. Every cylinder contains two ports for pumping in pressure air in different time phase. When one cylinder is pumped with air through one of the port, a pressure difference is generated in the cylinder and pushes the piston towards the opposite side at the lower pressure, resulting a torque about the rotation center.

Part	Component Name
1	Planetary gearbox
2	Supporting structure
3	Connecting bush
4	Cylinder
5	Shaft
6	Crank
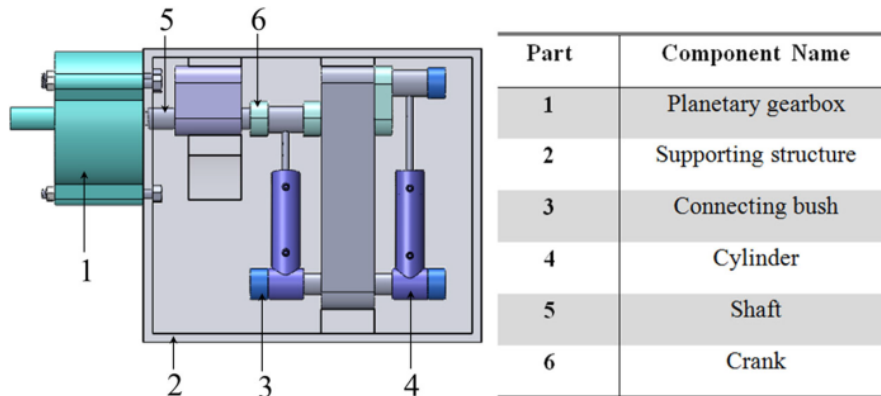
Figure 2. 11 A 3-D assembly view of the step motor by Yue Chen et al. consisting of six major components.[19]

Another much smaller pneumatic stepper motor was designed by Chen et al.[20] One purpose of this design is the compact size by reducing the number of components, therefore a 10mm diameter cylinder-shaped motor is presented. The CAD drawing and prototype are shown in Figure 2.12. The operation sequence can be compared with a spring ball pen. This design dramatically reduces the size of the actuator. However, one problem is that it can only in one direction actively.

No.	Part name	No.	Part name
1	Output shaft	5	Upper push rod
2	Outer guide pipe	6	Lower push rod
3	Spring	7	Air connector
4	Pin		
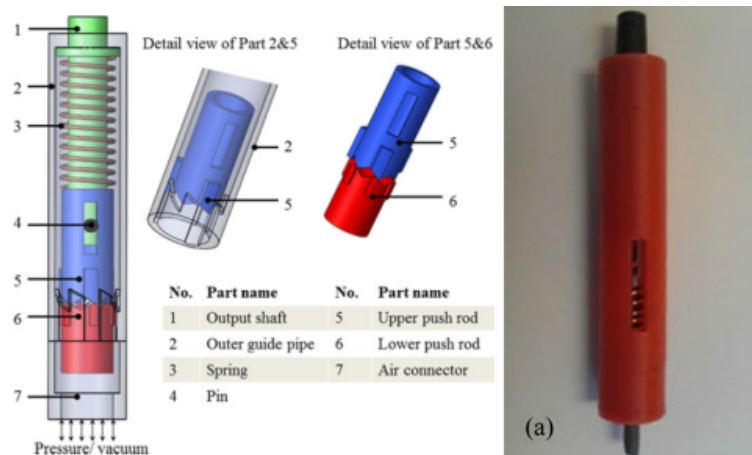
Figure 2. 12 Left: CAD drawing of the step motor by Yue Chen et al. Right: Prototype.[20]

Currently, the widely applied pneumatic actuators in MRI environment are step actuators, consisting of two types of gears, with one active and the other passive. The active gears push the passive gears sequentially providing rotational motions of the passive gears. Although only a limited number of actuators are mentioned in this section, a majority of other pneumatic step actuators still obey this driving principle. A comparison among the actuators mentioned in this section is shown in Table 2.2.

Table 2. 2 Comparison among different pneumatic step actuators.

Product	Actuator	Dimension (mm)	Complexity	Step size (deg)	Speed (rpm)	Torque (Nm)	SNR reduction (%)	Bidirectional/ Unidirectional
	Koichi Suzumori et al.[15]	Φ50×49	Simple	0.5	10	2	Not given	Bidirectional
	Hiroyuki Sajima et al.[16]	60×30×25	Simple	4.29	8.4	0.15	None	Bidirectional
	Dan Stoianovici et al.[17] [18]	85×30×30 70×20×25	Most complex	3.333	166.6	0.64	Not given	Bidirectional
	Yue Chen et al.[19]	Not given	More complex	3.6	2.4	0.8	2.35	Bidirectional
	Yue Chen et al.[20]	Φ10×60	Simple	60	90	0.0024	2.49	Unidirectional

2.3 MRI Compatible Materials

There are some limitations introduced by MRI environment when selecting materials. In MRI, when high quality images are to be obtained, an intense and homogeneous static magnetic field in the order of several Teslas is required to magnetize the hydrogen protons in the patient's body. And this static field will produce forces and torques on ferromagnetic or paramagnetic materials inside the scanner room.[21] Many materials used in conventional robotic and mechatronic systems, which have desirable mechanical properties such as strength and rigidity, are ferromagnetic.[4] These materials are not suitable in the MRI environment. Alternative MRI compatible materials should be nonmagnetic and nonconductive materials.

General Electric (GE) classifies several materials depending on the material's magnetic susceptibility (χ).[22] The selection of materials inside the MRI scanner room depends on the location of the elements, but the materials should generally be either diamagnetic ($\chi<0$) or slightly paramagnetic ($0<\chi<0.01$).[21] For materials in the imaging volume, the material susceptibility should be close to human tissue (-0.95ppm) and air (0.36ppm).[21][22] Materials ranging into this range can still be subclassified into three groups depending on the material's magnetic susceptibility difference form that of water ($\Delta\chi$):[22][23]

Group 1: Materials with essentially no detectable image artifacts when inside tissue.

Group 2: Materials with noticeable but insignificant image artifacts.

Group 3: Materials with easily noticed artifacts, but acceptable in certain locations and in smaller quantities.

Table 2.3 shows some materials subclassified into the three groups.

Table 2. 3 Materials magnetically compatible with MRI.		
Group 1 $\|\Delta\chi\| < 3ppm$	nylon, silicon nitride, teflon, polysulfone, magnesia, steatite, carbon fiber composites, vespel (acetal), plexiglass, zirconia, PEEK, wood, copper, etc.	
Group 2 $\|\Delta\chi\| < 10ppm$	alumina, silicon, quartz, lead, zinc, brass, etc.	
Group 3 $\|\Delta\chi\| < 200ppm$	titanium, molybdenum, tungsten, graphite, carbon fiber composites, tantalum, zirconium, bismuth, aluminum, etc.	

Safety is another crucial concentration introduced by MRI environment. The typical static magnetic field in current scanners is of 1.5-3 Tesla (up to 7-8 Tesla available for research).[24][25] In such a static magnetic field, ferromagnetic components would be strongly attracted, which is called missile effect.[24][25][26] Beyond damaging the equipment, the missile effect also injures people who are between the ferromagnetic equipment and the MRI scanner. Missile effect also introduces other serious hazards, such as twisting and dislocating metallic components in electronics, power tools and surgically implanted medical devices.

When moving the conductive materials in the fringe-field of the magnet field or switching magnetic field gradients, eddy current will be induced in the materials.[25][26][27] The eddy current results in heating of the element, consequently causing burns.[28] On the other hand, the generation of eddy current inside conductive materials may cause image artifacts. Non-conductivity of the material is therefore another factor to consider when selecting materials.

2.4 MRI Compatible Sensors

In the area of robotized MIS, the accuracy and safety require position and force sensors respectively, and as other devices introduced in the MRI environment, the sensors need to be MRI compatible as well.[21][4]

To track the position of the device, optical encoding technology is usually required, and conventional models tend to include ferrous materials need to be adapted for use inside the scanner room.[21] Elhawary et al.[29] developed a 1-DoF robotic module using surface mount incremental optical encoder from the EADR-8000 series with the size of the encoder sufficiently small (6.2×4.4×3.2mm) so that the incompatible material contained in the device only produces a small artifact. Mechanical encoders such as potentiometers can still be used to detect the position but must be made by non-magnetic materials and are generally placed outside the scanner bore,[21] such as the potentiometers JC22E (Nidec Copal Electronics Corp., Tokyo, Japan) installed in an endoscope manipulator for trans-nasal neurosurgery developed by Koseki et al.[30]

The principle widely applied in the design of MRI compatible force sensor is to detect the deformation of a flexible structure imposed due to the applied force. Tada et al.[31] developed an optical 2-axis force sensor that removes all magnetic materials from the sensor part and detects the displacement of a flexible frame by measuring the amount of light received by four photo sensors. The principle is shown in Figure 2.13. Similar principle can be witnessed in the device developed by Gassert et al.[24] that an optical sensor is applied to detect the displacement of a flexible hinge spring, which can be used to measure the imposed force based on the reflected light intensity over optical fibers. Tada and Kanada[32] developed another force sensor based on 2D optical micrometry, in which, the force is detected through the displacement of a thick plate, which works as flexible structure.

The optoelectronic components of the sensors could be disturbed by the MRI scanner[33] and introduce noise into the feedback and image.[21][33] The solution applied by several systems to deal with this problem is to pick up signals and transmit via fiber optic cables outside the scanner room.[29][30][33][34][35][36]
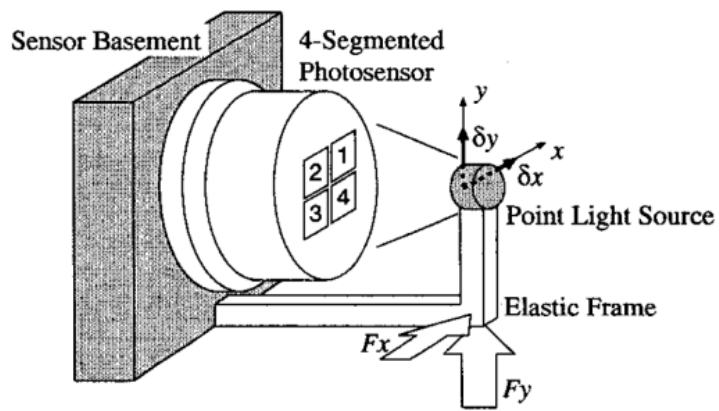
Figure 2. 13 Principle of optical force sensor by M. Tada et al.[31]

3. Robot Design

This chapter describes the steps of the robot design: Firstly the requirements of McRobot are discussed. Then the conceptual designed previously is introduced, based on which, a kinematic model is created. The kinematic model transforms the requirements of the tool tip to that of the actuator. The actuator is designed afterwards based on these requirements. As modular design reduces the cost and complexity during the design, it is therefore preferable to apply the same type of actuators for all DoFs. As the conceptual mechanism design was previously finished by dividing the robot into several main elements,[37] this chapter then describes the detailed designs of these main elements. Lastly, the overall design of the robot is represented.

3.1 Functional Requirements

A MoSCoW (Must Should Could Won't) list has been made to prioritize the requirements based on the studies around the word[37][38][39][40][41][42][43][44] and is modified as following after discussion with supervisors as shown in Table 3.1.

Table 3. 1 MoSCoW for McRobot.

Must	Closed bore MRI compatible(Compact size compatible between the patient and bore (within 18.5mm))
	Applicable for chest/thorax
	Applicable for different sized tools (0.71-2.1mm)
	Tool release mechanism
	Passive/Active mode switch
	Back-drivability
	Sterilizability
	Patient motion compensation passively (coughing and sneezing etc.)
	Active DoFs control: orientation, rotation, insertion
	Tool tip precision (3mm)
	Insertion force 4N
	Insertion speed 5mm/s
	Allowance for 'waggling' of the tool
Should	Tool tip precision (1mm)
	Insertion force: 10N
	Rotation/axial toque: 60Nmm
	Applicable for abdomen
	CT and PET compatible
	Center of motion on the skin
	Modular design
Could	Fast needle insertion
	Applicable for prostate, skull or brain
	Speed control for insertion
	Automated specimen remove and storage
	Respiratory motion compensation actively
Won't	Three translational actuated DoFs

Some explanations regarding the requirements are represented as following.

3.1.1 MRI and Size Compatibility

As mentioned in previous sections, there are limitations introduced by MRI environment when selecting materials. MRI compatible materials are nonmagnetic and nonconductive materials. What is more, as it is proposed to make a prototype in the lab RaM, the materials should be 3D printing or laser cut available. Except the material limitation, the compact size inside the MRI bore introduces another challenge for design. A study by Eftychios G.

Christoforou et al.[38] shows that a typical geometric limitation inside the MRI bore, as shown in Figure 3.1. A typical vertical working space between the patient and MRI bore is 18.5-23cm, which means the height of the robot must be limited within this size to manoeuvre smoothly. Mostly, MRI compatible devices are CT and PET compatible as well.
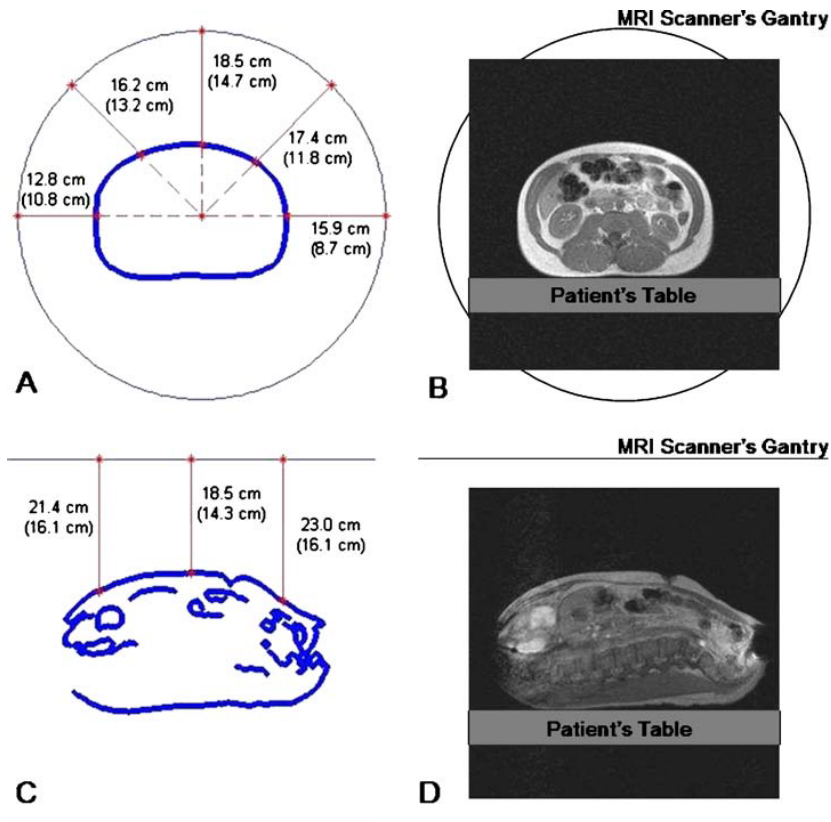
Figure 3. 1 Analysis of the available space with a human subject inside a cylindrical MRI scanner. A. Available space around the subject. B. Transverse MR image of the abdominal area. C. Available space above the subject. D. MR image of the abdominal and thoracic area.

3.1.2 Active DoFs and Human Motion Compensation

The compensation of the unexpected motions of the patient, due to respiration, coughing, sneezing and other faster and more unpredictable motions, is an important issue when designing the image guided surgery robot for MII.

Two kinds of motions are introduced in [11]:

One is the vertical motion of the patient's chest due to respiration. One solution to compensation this motion is to employ closed loop control to sense the chest motion actively and move the robot accordingly in order to retain the needle moving relatively to the patient. This is an acceptable method for the robots that are attached to a fixed plate, the patient couch, for example. However, it has been proved that, due to the low frequency of MRI scanner, to compensate the patient's motion by a closed loop control is not possible so far.[37] Another simpler and more reliable solution is to mount the device directly to the patient so that it moves passively with patient while remaining attached to the patient. The concept to mount the device to the patient can be witnessed in [11][12].

A similar concept was applied in the system developed by Bricault et al.[10], in which, a patent invented by Philippe Cinquin et al.[45] was applied which is a structure disposed over the patient's body and follows the patient's abdomen or thorax surface. This concept also provides an intrinsic compensation for some unwanted motions of the patient. What is more, in the system by Bricault et al.[10] the needle is grasped and when being released by the

14

clamps, the needle can then follow the motions of the target organ of the patient, therefore avoiding injury.

The second motion is the oscillation of the needle. When the needle in inserted inside the body, the outside part is observed to wave due to the relative motion between respiratory tissues and skin, which is referred to as waggling. If the needle is fixed from outside to stop the oscillation, the tissue will be lacerated by the needle. A release mechanism can be introduced to allow the needle to freely waggle, which can be read in [10][11].

Another solution that can contribute to the safety is to make the robot more compliant, using flexible elements, etc., allowing the robot follow the motions of patient. However, flexible element may cause some problems, for example, the flexibility in unwanted directions, or the varying torques during bending and complexities in the control system.

To compensate the human motion passively, a patient-mounted concept is chosen as the structure of McRobot. Therefore the first prototype proposed contains four active DoFs, which are two orientations, one insertion and one rotation. The mounting of the robot on the insertion point can be achieved manually, which means three translational DoFs can be therefore omitted.

The reason that a rotational DoF is in Must Have is due to the needle deflection that has been observed in many systems with bevelled tip needles, which is the primary source of needle placement error.[39][40][41][42] In this application, rotational DoF is used for steering the needle to limit its deflection and bypass vital tissues.

3.1.3 Application for Different Sized Tools

The sizes of needles for different tasks range with diameters of 0.71-2.1mm and insertion lengths of 0-150mm.[43] Therefore a tool grip compatible with several sized tools is a Must Have requirement.

3.1.4 Force, Torque and Velocity

Okamura et al.[44] performed an experiment showing that to insert a needle into a bovine liver, a maximum force of approximate 3.5N was observed. Another experiment was performed by Walsh[41] to insert the needle into a deceased turkey, and a maximum force of approximately 4N for insertion through the chest wall and into the lung was measured. Furthermore, The study by Walsh mentioned a discussion with doctors at MGH revealed that for some applications (e.g. larger needles and probes), a higher force may be needed. In Walsh's design, a needle insertion force of about 10N was used as the design specification. In this McRobot study, 20N is used for the safety and function reason.

In the study by Walsh, it also determined the torque required to orientate a needle when it is inserted into a patient, which were 25Nmm and 60Nmm at needle insertion depths of 50mm and 100mm respectively. The torque increases with the increasing insertion depth.

Several studies mention that the desired velocity of the tool is in the range of 5-10mm/s to 50mm/s. In this McRobot study 5mm/s is used as desired velocity.[37]

3.1.5 Precision

Hsuan et al.[46] presented a quality assessment of high spatial resolution for MRI showing that the resolution of a high resolution MRI system (1.5T) can be from 0.1 up to 1.5mm. The thesis by Hoogen[37] represents that a common closed bore MRI imager (3T) can achieve a spatial resolution of 3mm. The precision of McRobot is desired to be approximate 1mm. A robot with higher precision is not necessary as it cannot be distinguished by most imagers.

3.1.6 Passive/Active Mode Switch

When the actuator is in off mode, the robot can still be operated and moved passively. As friction exists inside the robot, it keeps the robot in the position and compensates gravity.

3.2 Robot Kinematics

A concept was decided previously by the researcher Foad Sojoodi Farimani and his former students as shown in Figure 3.2. With this conceptual design, the kinematic model of the robot can be analysed.

3.2.1 Conceptual Design

As shown in Figure 3.2, it is a 4-DoF patient mounted robot. The insertion angle manipulation is based on driving the length of three ropes. The tool (a needle) is gripped in a carriage, which translates over guidance. The base contains three flexible legs. Three actuators are fixed on the legs to active two orientation DoFs, and two actuators are fixed on the carriage to active the insertion and rotation DoFs.
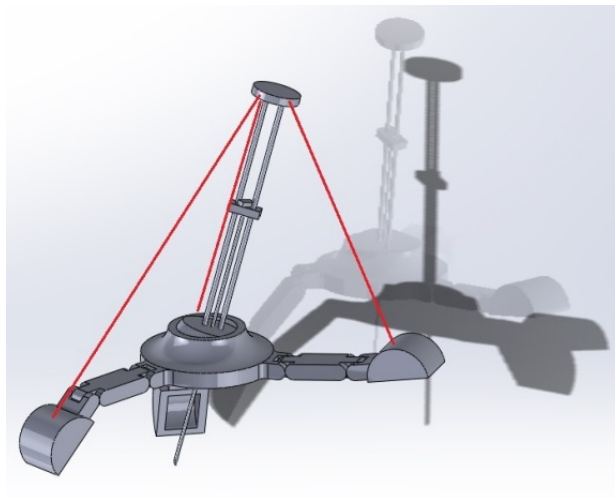
Figure 3. 2 McRobot conceptual design.

The operative mode of the McRobot that is positioned on the patient is shown in Figure 3.3.
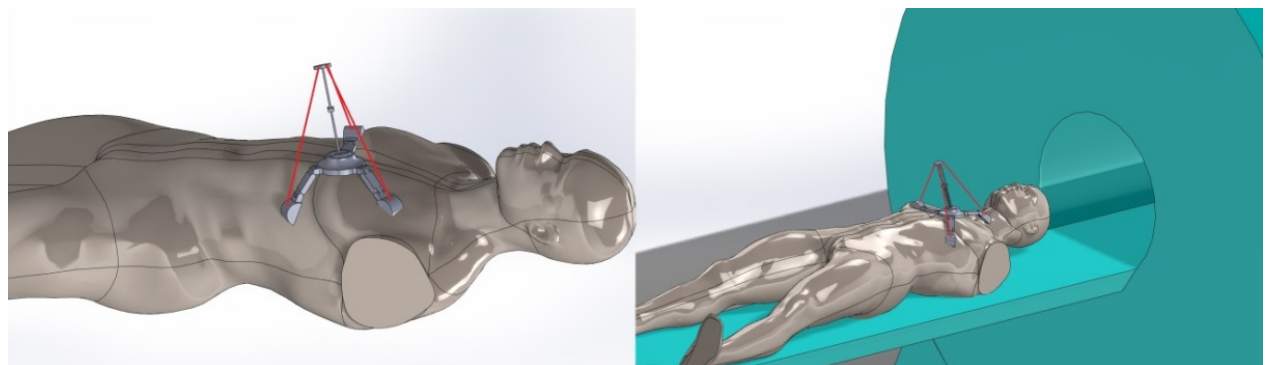
Figure 3. 3 McRobot positioned on the thorax of the patient inside a closed MRI bore.

3.2.2 Kinematic Model

To transform the requirements of the tool tip to that of the actuator as the precondition of actuator design, a kinematic model is created and simplified as shown in Figure 3.4. In the kinematic model, the three ropes are assumed to connect at a common point on top of the tool guide.
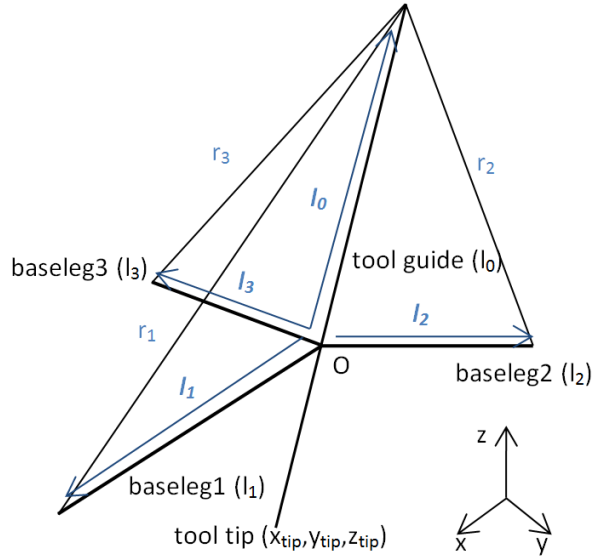
Figure 3. 4 Kinematic model of McRobot.

The location of the needle tip is represented by $(x_{tip}, y_{tip}, z_{tip})$, with O the coordinate frame origin located at the center of motion. x-axis is aligned with baseleg 1, and z-axis points upwards in vertical direction. The vectors $\mathbf{l_1}$, $\mathbf{l_2}$, and $\mathbf{l_3}$, starting from the origin, represent the directions and lengths of the three baselegs. The vector $\mathbf{l_0}$ represents the guide of the tool, starting from the origin and ending at the common point of the ropes. α represents the angle between the tool guide and z-axis, and β represents the angle between the projection of tool guide on the x-y plane and x-axis, as shown in Figure 3.5.
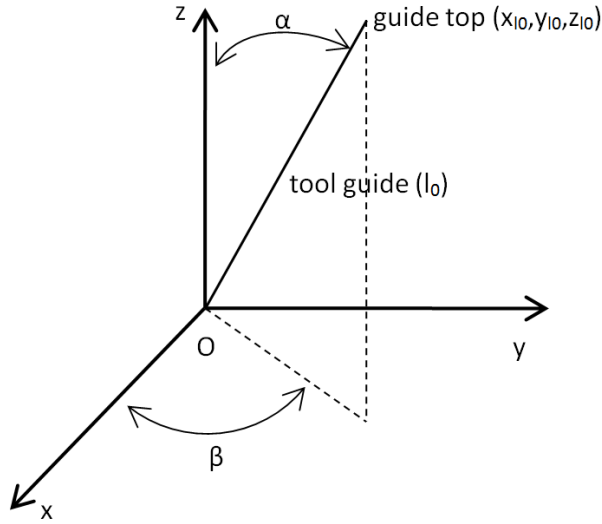
Figure 3. 5 Definitions of α and β.

The position of the tool guide top can be obtained:

$$x_{l0} = l_0 \sin \alpha \cos \beta$$

$$y_{l0} = l_0 \sin \alpha \sin \beta$$

$$z_{l0} = l_0 \cos \alpha$$

In which, l_0 represents the length of the tool guide, which is a constant.

Assume the actuated ropes have the lengths of r_1, and r_2, respectively, therefore:

$$r_1 = k_1 \theta_1 = |\mathbf{l_1} - \mathbf{l_0}| = \sqrt{(x_{l1} - l_0 \sin \alpha \cos \beta)^2 + (y_{l1} - l_0 \sin \alpha \sin \beta)^2 + (z_{l1} - l_0 \cos \alpha)^2}$$

$$r_2 = k_2 \theta_2 = |\mathbf{l_2} - \mathbf{l_0}| = \sqrt{(x_{l2} - l_0 \sin \alpha \cos \beta)^2 + (y_{l2} - l_0 \sin \alpha \sin \beta)^2 + (z_{l2} - l_0 \cos \alpha)^2}$$

In which, θ_1, θ_2 represent the rotation angles of the actuator that fixed on the legs. k_1, k_2 represent the linear relation between the actuator rotation angle and rope displacement. x_{li}, y_{li}, z_{li} (i = 1, 2) represent the coordinates of baselegi.

The position of the tool tip can be obtained as following:

$$x_{tip} = -l \sin\alpha \cos\beta$$

$$y_{tip} = -l \sin\alpha \sin\beta$$

$$z_{tip} = -l \cos\alpha$$

In which, l represents the depth of the insertion and can be obtained by:

$$l = k_0 \theta_0$$

In which, θ_0 represents the rotation angle of the actuator for insertion. k_0 represents the ratio between the insertion depth and rotation angle of the corresponding actuator.

Therefore:

$$x_{tip} = -k_0 \theta_0 \sin\alpha \cos\beta$$

$$y_{tip} = -k_0 \theta_0 \sin\alpha \sin\beta$$

$$z_{tip} = -k_0 \theta_0 \cos\alpha$$

The following relation can be obtained through above simultaneous equations:

$$\begin{bmatrix} x_{tip} \\ y_{tip} \\ z_{tip} \end{bmatrix} = \mathbf{f}\left(\begin{bmatrix} \theta_1 \\ \theta_2 \\ \theta_0 \end{bmatrix} \right)$$

The coordinate of tool tip can be represented by:

$$\mathbf{X} = \left(x_{tip}, y_{tip}, z_{tip} \right)$$

And the joint positions of the actuators can be represented by:

$$\mathbf{Q} = (\theta_0, \theta_1, \theta_2)$$

Therefore:

$$\mathbf{X} = \mathbf{f}(\mathbf{Q})$$

The Jacobian matrix maps the joint velocities to the tool velocities, and a tiny displacement of the joint to that of the tool tip:

$$\mathbf{J_{ij}} = \frac{\partial x_j}{\partial q_i}$$

In which, **J** represents the Jacobian matrix and is derived as following:

$$\mathbf{J} = \begin{bmatrix} \dfrac{\partial x_{tip}}{\partial\theta_0} & \dfrac{\partial x_{tip}}{\partial\theta_1} & \dfrac{\partial x_{tip}}{\partial\theta_2} \\ \dfrac{\partial y_{tip}}{\partial\theta_0} & \dfrac{\partial y_{tip}}{\partial\theta_1} & \dfrac{\partial y_{tip}}{\partial\theta_2} \\ \dfrac{\partial z_{tip}}{\partial\theta_0} & \dfrac{\partial z_{tip}}{\partial\theta_1} & \dfrac{\partial z_{tip}}{\partial\theta_2} \end{bmatrix}$$

The precision can be represented as following:

$$\begin{vmatrix} \delta x_{tip} \\ \delta y_{tip} \\ \delta z_{tip} \end{vmatrix} = \left\| \mathbf{J} \begin{bmatrix} \delta\theta_1 \\ \delta\theta_2 \\ \delta\theta_0 \end{bmatrix} \right\| = 1mm$$

As the application of modular design, the step motions of actuators are same. Therefore:

$$\delta\theta_0 = \delta\theta_1 = \delta\theta_2$$

In the former thesis by Hoogen, the passive revolute joints of the baselegs were assumed to have an angle of zero degrees. The lengths of baseleg and tool guidewere calculated as 157.25 mm and 185 mm respectively.[37] Therefore:

$$x_{l1} = 157.25$$
$$y_{l1} = z_{l1} = 0$$
$$x_{l2} = -78.62$$
$$y_{l2} = 136.18$$
$$z_{l2} = 0$$
$$l_0 = 185$$

3.3 Actuator Design

With the kinematic model, the requirements of the actuator can be determined. The actuator can be therefore designed based on these requirements.

3.3.1 Actuator Requirements

Three requirements, which are step motion, space, and output torque, are decided for the actuator based on the requirements of robot.

3.3.1.1 Step Motion

By analysing the kinematic model, it can be indicated that the step motion of the actuator is:

$$\delta r_i = k_i \delta\theta_i = 0.9999 \text{mm}, \qquad (i = 1,2)$$

In which, $\delta\theta_{1,2}$ represent the step motion of the actuator. $k_{1,2}$ represent the linear relation between the actuator rotation angle and rope displacement, indicating the diameter of the output shaft geometrically. To modify $\delta\theta_{1,2}$ to a reasonable values and guarantee that there is enough space for the ropes to be twined, $k_{1,2}$ are modified to be 5mm, which leads to a step motion of:

$$\delta\theta_i = \frac{0.9999}{5} \text{rad} = 0.1999 \text{rad} = 11.46^\circ, \qquad (i = 1,2)$$

3.3.1.2 Speed

As the step motions of actuators are same:

$$\delta\theta_0 = \delta\theta_1 = \delta\theta_2$$

Therefore:

$$\delta\theta_0 = 11.46^\circ$$

When the orientation of the arm is fixed, the insertion speed only depends on the insertion actuator, which is fixed in the tool guidance system. This speed can be represented through a ratio between the tool tip precision and the step motion of the actuator, which is k_0:

$$k_0 = \frac{p}{\delta\theta_0} = \frac{1}{11.46} \text{mm/}^\circ = 0.08726 \text{ mm/}^\circ = 5.002 \text{ mm/rad}$$

In which, p represents the precision of the tool tip. The relation between the insertion speed and output speed of actuator can be represented as:

$$k_0 = \frac{v}{\omega}$$

In which, v represents the velocity of the tool tip and ω represents the output speed of actuator. In this study 5mm/s is used as desired velocity. Therefore:

$$\omega = \frac{v}{k_0} = \frac{5\,\text{mm/s}}{0.08726\,\text{mm/°}} = 57.30\,°/s = 0.9996\,\text{rad/s}$$

3.3.1.3 Output Torque

Study by C. J. Walsh indicates that in general, a force of minimum 4N is required for the tool tip to insert through the skin and soft tissue, and for some applications, a tool tip force up to 10N is required.[41]

Similarly with the assumption when analysing output speed: when the orientation of the robot is fixed, the insertion force is only generated by the insertion actuator, which is fixed in the tool guidance system. The relation between the insertion force and output torque of actuator can be represented as:

$$T = Fk_0 = 10{\times}5.002\text{Nmm} = 50.02\text{Nmm}$$

The requirements of the actuator are shown in Table 3.2.

Table 3. 2 Actuator requirements.

Step motion (°)	Speed (rad/s)	Torque (Nmm)
11.46	0.9996	50.02

3.3.2 Actuator Conceptual Design

The step rotational motion is realized by two types of gears, which are rotor and pistons with the same tooth size. The arrangement of these main components is shown in Figure 3.6. The working principle of the actuator is presented in Figure 3.7.
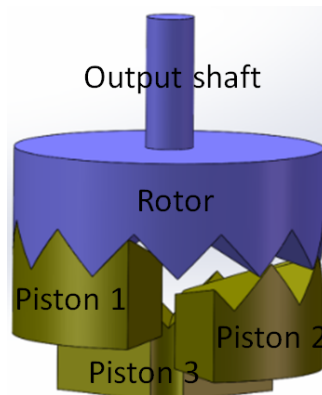
Figure 3. 6 Main components of the actuator.
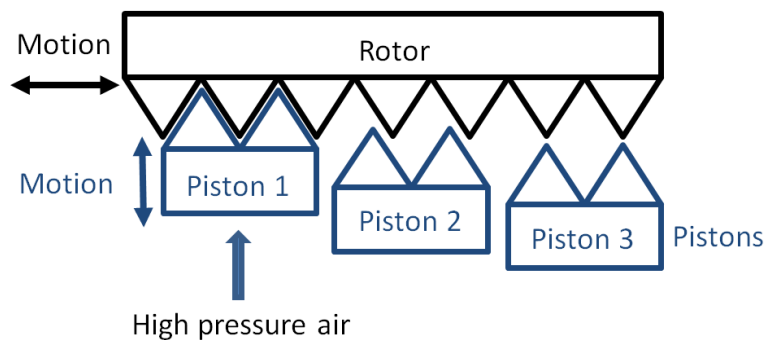
Figure 3. 7 Schematic principle representation.

The working process of this actuator can be explained as: First, postion 1 is pushed by high pressure air consequently the rotor rotates and engages with piston 1. Then, piston 2 is pushed up and the rotor rotates one more step. At the same time, piston 1 is pushed down by a return mechanism. Similarly, piston 3 is pushed up and the rotor rotates one more step again, while piston 2 is pushed down. By the repetition of this operation, the rotor continues

rotating. The rotation direction can be easily switched by changing the pushing sequence of pistons.

To return the piston to its zero position after meshing and reduce the number of required hoses, flexible material, such as a rubber bar, is used as a spring, pushing the piston back.

3.3.3 Actuator Requirements Realization

When the requirements are determined, the actuator can be designed by hardware based on the requirements. The step motion of the actuator depends on the size of the rotor, especially the tooth pitch of the teeth on the rotor. The rotation speed depends on the frequency of valves. And the output torque depend on the cooperation of the shape of teeth on the rotor and pistons, the cross sectional area of pistons, the applied air pressure, and the characteristic of the flexible materials that working as the return mechanism.

3.3.3.1 Rotor Size

Considering the limited dimension for the actuator, introduced by the compact space in the MRI scanner, the diameter of the rotor is adjusted to be 25mm. A smaller diameter will result in difficulties to achieve the required output torque, while a larger dimension will increase the weight of the robot and reduce its geometrical compatibility with the MRI scanner. The circumference of the rotor can be obtained by:

$$C = \pi d = 3.14 \times 25mm = 78.50mm$$

In which, C and d represent the circumference and diameter of the rotor respectively.

Therefore, the arc length of the rotor corresponding to the step motion is represented as:

$$\delta L = \frac{\delta \theta_i C}{2\pi} = \frac{0.1999 \times 78.50}{2 \times 3.14} mm = 2.499mm, \qquad (i = 1,2)$$

In which, δL represents the arc length of the rotor corresponding to a step motion, which is one third length of the tooth pitch, as shown in Figure 3.8.
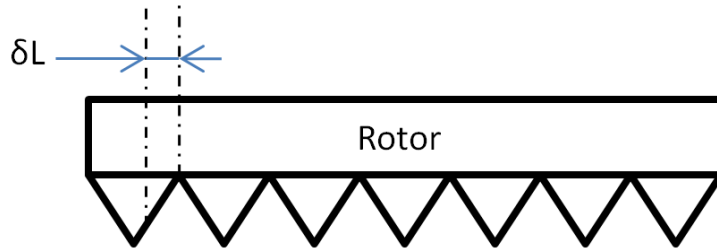
Figure 3. 8 Arc length corresponding to a step motion δL.

Therefore the tooth pitch P is represented as:

$$P = 3\delta L = 3 \times 2.499mm = 7.497mm$$

In the kinematic model analysis, the linear relations k_1, k_2 are introduced. Mechanically, k_1 and k_2 represent the linear relation between arc length and central angle of the rotor, and can be represented by the diameter of the output shaft:

$$k_i = \frac{d_{shaft}}{2}, \qquad (i = 1,2)$$

The teeth on both rotor and pistons have the same tooth pitch, so that they can mesh perfectly.

In which, d_{shaft} represents the diameter of the output shaft. As k_1 and k_2 are set to be 5mm, the diameter of the output shaft is therefore 10mm.

3.3.3.2 Force Analysis

The force analysis model of the rotor and piston is as shown in Figure 3.9.
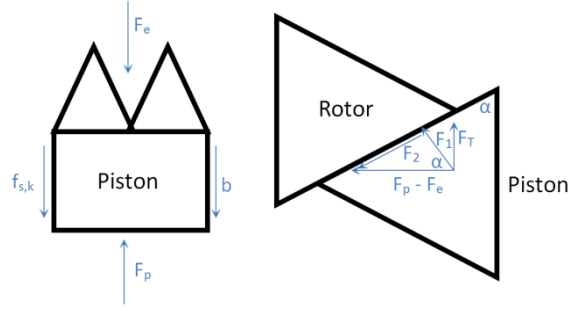
Figure 3. 9 Force analysis of rotor and piston.

In which, $f_{s,k}$ represent the friction coefficients of static friction and kinetic friction between the piston and cylinder. b represents the viscosity coefficient when lubrication is applied. F_p represents the thrust force received by the piston from the high pressure air. F_e represents the elastic force generated by the flexible material when being compressed as a return mechanism. As the friction between the piston and cylinder is small compared to the thrust force and elastic force, and no lubrication is applied currently, both $f_{s,k}$ and b are therefore neglected to simplify the calculation. F_1 and F_2 represent the component force of the interaction force between two teeth, which is F_p-F_e, in the orthogonal directions. F_T represents the tangential force received by the rotor that rotates the rotor around its axis. α represents the base angle of tooth.

The piston received force F_p from high pressure air can be represented as:

$$F_p = Ap$$

In which, A represents the cross-section area of piston. p represents the air pressure of high pressure air. The relation between the actuator output torque T and force in the tangential direction F_T, received by the rotor, can be represented as:

$$F_T = \frac{T}{r_{avg}}$$

In which, r_{avg} represents the average radius of output shaft, which can be assumed as r/2, where r represents the radius of rotor, which 12.5mm.

From the force analysis in Figure 3.9, to overcome the friction and achieve effective motions of rotor and piston, the shearing force on the tooth surface should larger than the friction between the tooth surfaces:

$$F_2 = \mu F_1$$

In which, μ represents the friction coefficient between the tooth surfaces of rotor and piston. Coulomb friction is the only interaction.

From the force analysis of piston and rotor separately, the following equation and inequation can be obtained:

$$F_p - F_e = F_1 \cos \alpha + F_2 \sin \alpha$$

$$F_T \leq F_1 \sin \alpha - F_2 \cos \alpha$$

Equality holds when the acceleration of the piston is neglectable. Therefore:

$$F_p - F_e = F_1 \cos \alpha + \mu F_1 \sin \alpha = F_1 (\cos \alpha + \mu \sin \alpha)$$

To avoid the self-lock, the following inequations need to be satisfied:

$$(F_p - F_e) \sin \alpha > \mu (F_p - F_e) \cos \alpha$$

$$\tan\alpha > \mu$$

Two methods can satisfy these conditions. One is to adjust the tooth base angle. The other one is to introduce lubrication to adjust the friction coefficient. However, the friction coefficient is difficult to measure currently. Therefore, it is properly assumed to be 0.5. The base angle of teeth α is currently adjusted to be 45°. Pointed teeth will result in high rotational accuracy but meanwhile thinner tooth pitches. When the tooth pitches are too thin, any small lateral motion of piston will cause the actuator fail. Otherwise, if the accuracy is fixed, to guarantee this accuracy, more pointed teeth will result in longer tooth depths, causing larger elastic force from the flexible material and larger size of the actuator. Therefore, 45° is considered as a suitable angle.

One advantage of this angle is that, by this angle, when the return mechanism fails accidentally, it is still able to push back the piston by the rotor.

Simultaneous equations above lead to:

$$F_p - F_e = 24.01N$$

It is prefer to increase cross-sectional area of piston and reduce the air pressure to achieve F_p due to safety and sealing reasons. Considering the compact area available for the actuator, the cross-sectional area of piston is achieved to be 118.7mm². Larger cross-sectional area will result in a too thin cylinder wall. When the air pressure is adjusted to be 5bar:

$$F_e = F_p - 8N = Ap - 8N = 118.7 \times 0.5N - 24.01N = 35.34N$$

As the base angle of teeth is 45° and the tooth pitch is 7.497mm, the tooth depth D can be represented as:

$$D = \frac{P \tan \alpha}{2} = \frac{7.497 \times \tan 45°}{2} mm = 3.749mm$$

The stroke of a piston is adjusted to be 4mm, which is a little longer than the tooth depth to guarantee the smooth motion of the rotor relative to returned pistons. The stiffness coefficient of the flexible material, working as the return mechanism, can be represented as:

$$k_e = \frac{F_e}{\Delta x} = \frac{35.34}{4} N/mm = 8.835N/mm$$

In which, Δx represents the stroke of a piston.

The Young's modulus of the material can be represented as:

$$E = \frac{k_e L_0}{A_0}$$

In which, L_0 and A_0 represent the original length and cross-sectional area of the flexible material.

The original length and cross-sectional area of the flexible material can be adjusted to be 20mm and 9mm² to adapt the compact area in the actuator. Therefore:

$$E = \frac{8.835 \times 20}{9} N/mm^2 = 19.63N/mm^2 = 0.01963Gpa$$

This result indicates that it is possible to select a rubber bar (9mm² × 20mm) with Young's modulus of 0.01963Gpa as a return mechanism.

3.3.3.3 Valve Selection

The model of a single step motion can be represented as Figure 3.10. A rubber membrane is fixed on the underneath of piston, working as a diaphragm, to avoid the air leakage in the cylinder.
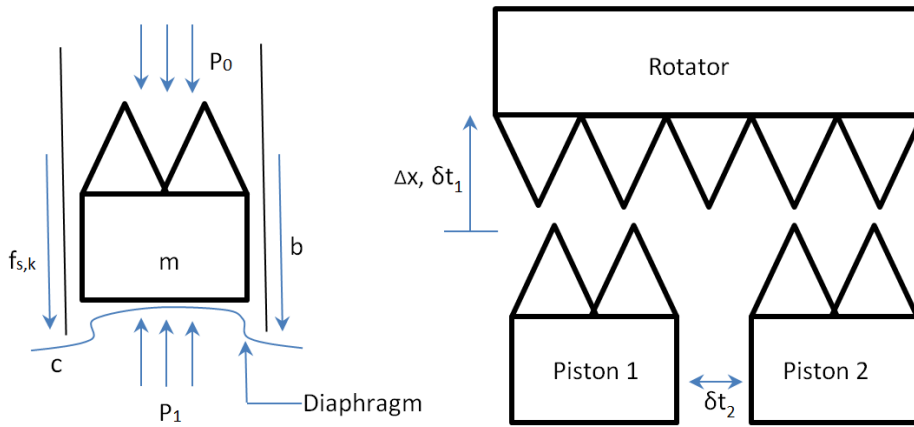
Figure 3. 10 Model of the step motion. Left: model of a single piston. Right: model of two adjacent pistons in cooperation with a rotor.

In which, P_0, P_1 represent the air pressure above and under the piston respectively. m represents the mass of a single piston. $f_{s,k}$ represent the friction coefficients of static friction and kinetic friction between the piston and cylinder. b represents the viscosity coefficient when lubrication is applied. c represents the stiffness coefficient of the diaphragm, which avoids the air leakage from air tube to the cylinder. Δx represents the stroke of a single piston. δt_1 represents the duration for a single piston to operate from its zero position to end position and then be pushed back to the zero position by the return mechanism. δt_2 represents the interval between the operations of two adjacent pistons.

The duration, δt, which is consumed to achieve a completed step motion, can be represented as:

$$\delta t > \delta t_1$$

For the further work, if a more precise motion analysis is required, all factors that introduced in the above model will be considered. Currently, they are neglected.

The output speed of the actuator can be represented as:

$$\omega = \frac{\delta \theta_i}{\delta t} = \frac{\delta \theta_i}{\delta t_2}, \qquad (i = 0,1,2)$$

The frequency of the operation of the pistons can be represented as:

$$f = \frac{1}{\delta t} = \frac{\omega}{\delta \theta_i} = \frac{0.9996 \, \text{rad/s}}{0.1999 \text{rad}} = 5.000 \text{Hz}, \qquad (i = 0,1,2)$$

The frequency of the pneumatic valve terminal cannot be too high, because the piston needs time to return to its zero position before the next positon to be activated. When selecting the pneumatic valve terminal, the frequency of the terminal should be no larger than 5Hz.

Five pneumatic actuators are required to activate the robot. Therefore fifteen pneumatic valves, or a valve terminal with at least fifteen outputs, are required to pressurize and decompress the cylinders of the actuators. The inputs of the valves are connected with the high pressure air source and the outputs are connected with the cylinders respectively. The outputs pressurize and decompress the cylinders in sequence in order to drive the actuators correctly.

3.3.4 Actuator CAD Design

The assembly, exploded view, and cross section of the actuator are shown in Figure 3.11-3.13. The screw on the surface of the shaft guides the rope so that the rope does not twine chaotically. The small ring on the surface of the rotor fixes the end of the rope. The groove on top of the output shaft fixes the transmissions such as a gear. Plastic balls are distributed

above and underneath the rotor, working as a ball bearing, to reduce the fiction. This friction can be controlled by tightening or releasing the screws. The return mechanism, which consists of three rubber bars, is integrated inside the actuator so that the design is more compact and nice-looking. The stroke of pistons is longer than the tooth depth of rotor and pistons so that the rotor does not contact the pistons which are in zero position, guaranteeing smooth rotation. A rubber membrane is fixed on the underneath of cylinders, working as a diaphragm, to avoid the air leakage from air tubes to the cylinders.
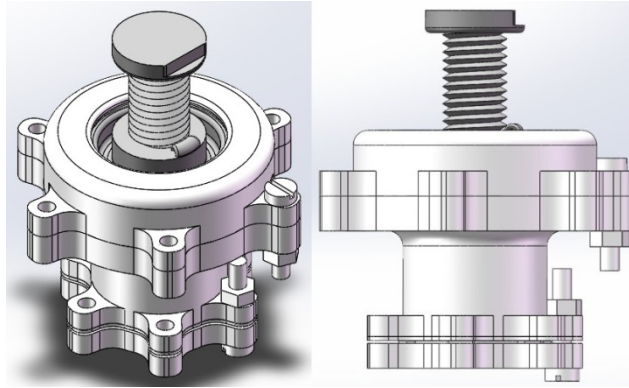
Figure 3. 11 Assembly of the actuator.
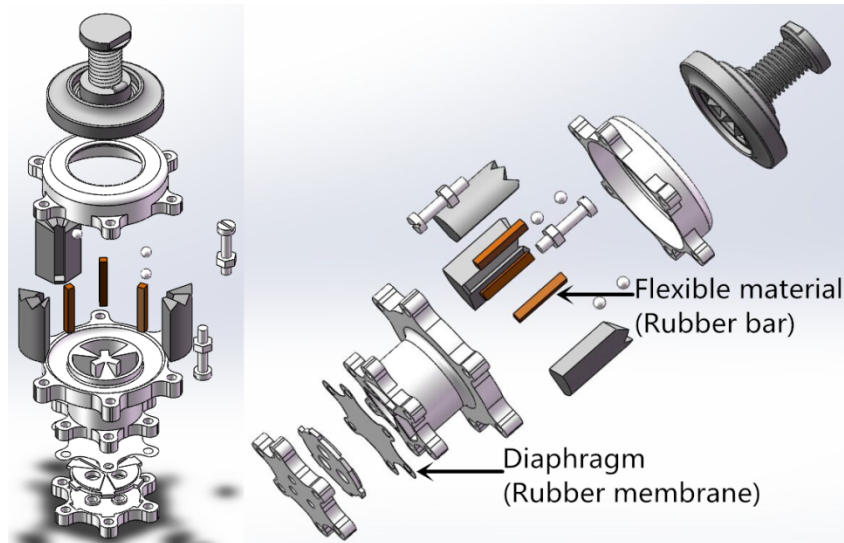
Figure 3. 12 Exploded view of the actuator.
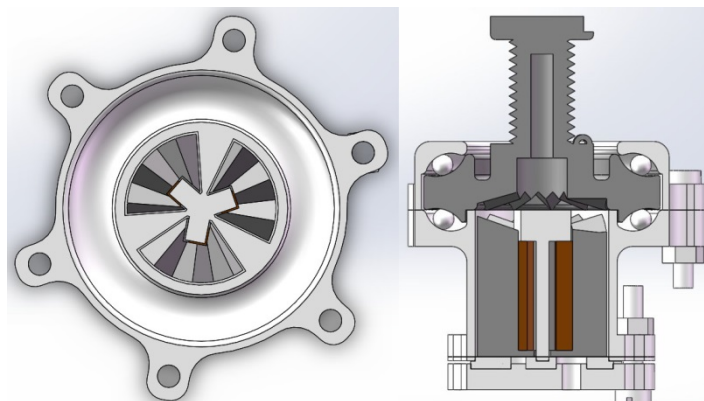
Figure 3. 13 Top and side cross section of the actuator.

3.4 Detailed Mechanical Design

After the overall conceptual design is determined, showing in Figure 3.2, detailed design of the robot can be proceeded. The main elements of the robot are: mounting method,

insertion angle manipulator, tool drive mechanism, base, and attachment method. The mounting method has already been decided to be a patient-mounted concept due to safety, size, reliability, and cost effectiveness reasons. The other elements are discussed in the following sections.

3.4.1 Insertion Angle Manipulator

The first element needed to design in detail is the insertion angle manipulator. It is determined in the MoSCoW list that the center of motion is a Should requirement as it avoids unexpected lateral motion of the tool in case of system malfunction and eases the control of the robot. A ball joint, working as a remote center of motion on the bottom of the mechanism, is therefore designed. The CAD model of the ball joint is shown in Figure 3.14. The friction between the ball and the shells can be controlled by the screws and nuts.
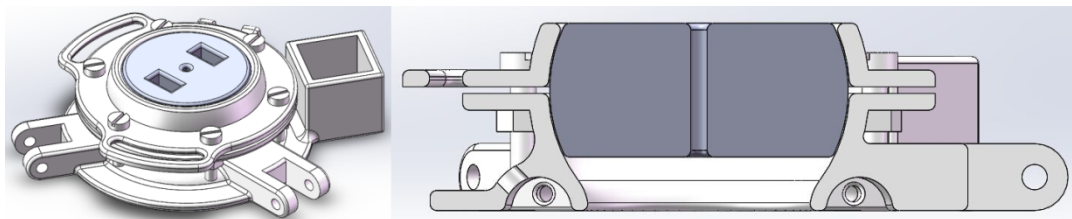
Figure 3. 14 Figure 3. 14 Left: Assembly of the ball joint. Right: Cross section of the ball joint.

The cubic groove on the side is to install the MRI contrast, which is shown in Figure 3.15.

Figure 3. 15 MRI contrast.

The insertion angle manipulator concept that consists of three ropes by Hoogen[37] is remained. Fishing lines are applied as ropes.

3.4.2 Tool Drive Mechanism

The next element to be designed after the insertion angle manipulator is the tool drive mechanism. The function of tool drive mechanism is divided into two parts: tool translation alone guidance and tool rotation around its axis, which are described respectively in the following sections.

3.4.2.1 Tool Translation

A comparison of tool translation based on friction rollers versus that based on a linear guidance technique was considered by Hoogen previously and the tool translation based on a linear guidance technique, which was a lead screw, was preferred for McRobot.[37] In this project, rack and pinion is considered to be more suitable due to its back-drivability, although the fact that rack and pinion means more weight on the carriage and a more complex carriage design, as the actuator driving the rack and pinion is fixed on the carriage. However, as back-drivability is the dominant criteria, rack and pinion is therefore still retained.

3.4.2.2 Tool Rotation

The functional requirement of the tool rotation around its axis can be achieved by coupling two bevel gears on the carriage. One advantage of this design it that the actuator can be

installed parallel with the carriage, which decreases the dead-zone of insertion. The overall arrangement of the bevel gears and the carriage, as well as the corresponding actuator and a zoom-in are shown in Figure 3.16.
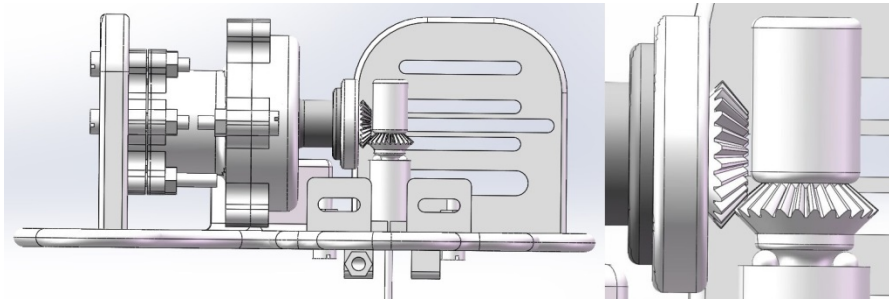
Figure 3. 16 Left: Arrangement of bevel gears, carriage, and actuator. Right: Zoom-in of the bevel gears.

It can be seen that the shaft of the actuator is shorter. This is because that this actuator does not drive or guide any rope, therefore a shorter shaft reduces the size.

3.4.3 Robot Base

The robot base should be able to adapt to various curves of different body regions to guarantee the versatility. A base that consists of three octopus biomimicry shaped baselegs, each baseleg consisting of two passive revolute joints, was determined by Hoogen.[37] The baselegs are connected by the ball joint. However, simulation shows that the versatility is not high enough if all the revolving shafts are parallel. Therefore on each baseleg, an extra revolute joint, containing two mutually perpendicular revolving shafts, is added, as shown in Figure 3.17.
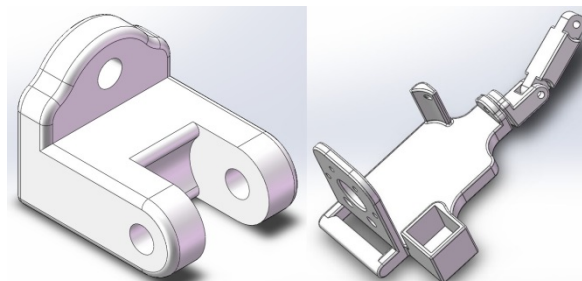
Figure 3. 17 Left: Extra revolute joint with two mutually perpendicular revolving shafts. Right: Assembly of a leg, containing the extra joint.

On the last section of the baseleg, a cubic groove is set to install the MRI contrast. Such cubic groove for MRI contrast can be seen on the carriage as well so that the depth of the insertion can be observed.

3.4.4 Attachment Method

Two attachment methods, which are pneumatic suctions and straps, are combined as the final attachment method. The pneumatic suction cups are arranged underneath the ball joint and baselegs. On the end of each baseleg, an attachment bar is added to connect the strap. The positions of pneumatic suction cups and attachment bar are shown in Figure 3.18.
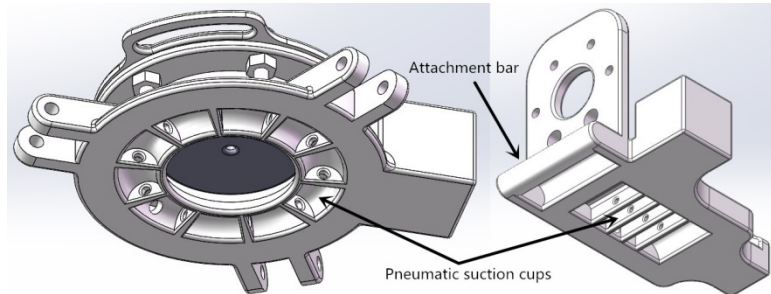
Figure 3. 18 Positions of pneumatic suction cups and attachment bar.

3.5 Final Design

In summary, the details of a 4-DoF patient-mounted MRI compatible robot have been designed. The insertion angle manipulation is based on a ball joint which is driven by three ropes. Rack and pinion is chosen as the tool guidance. The tool rotates through two coupled bevel gears, which transform the rotation of the actuator shaft to that of the tool. The base that consists of three octopus biomimicry shaped baselegs, each baseleg containing a revolute joint with two mutually perpendicular revolving shafts, is applied. Both pneumatic suctions and straps are applied as the attachment method. Four small ball bearings are applied to constrain the unwanted DoFs of the carriage and reduce the friction between the guidance and carriage. Consequently, the carriage translates along the guidance smoothly. The final detailed CAD model is shown in Figure 3.19.
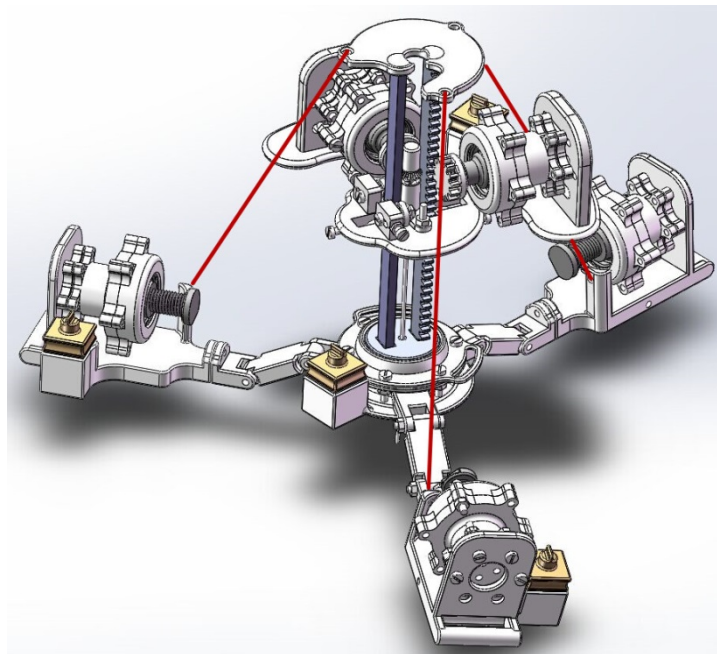
Figure 3. 19 Final CAD moedl of the robot.

4. Prototype and Test

The functional prototypes of the pneumatic actuator and robot are produced in the RaM[1] lab by 3D printing and laser cutting equipment. The main structure of the actuator is made out of resin. The robot is mainly made out of ABS and Delrin. The actuator and robot are tested in both lab RaM and a real MRI scanner.

4.1 Prototype

The prototype of the pneumatic actuator is shown in Figure 4.1. The main components, the rotor and pistons, as well as the cylinder and head cover, are 3D printed out of resin. The screws, nuts, and shims are used to control the friction in the ball bearing. In which, the screws and nuts are made out of nylon. The shims are laser cut out of polyester. The diaphragm is made out of latex, and cannot be laser cut therefore cut by hand.
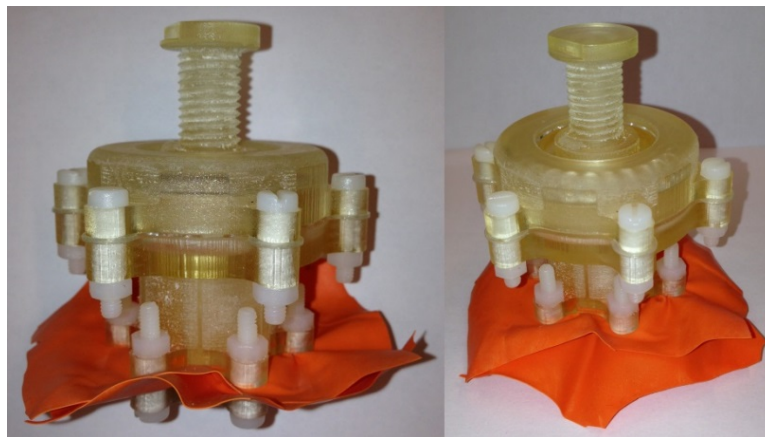
Figure 4. 1 Prototype of the pneumatic actuator.

The prototype of the whole robot is shown in Figure 4.2. The ball joint (white), baselegs (black), carriage (white), and top plate (white) are 3D printed out of ABS. The guide rail (black) and rack (black) are laser cut out of Delrin. The tubes are made out of polyurethane.
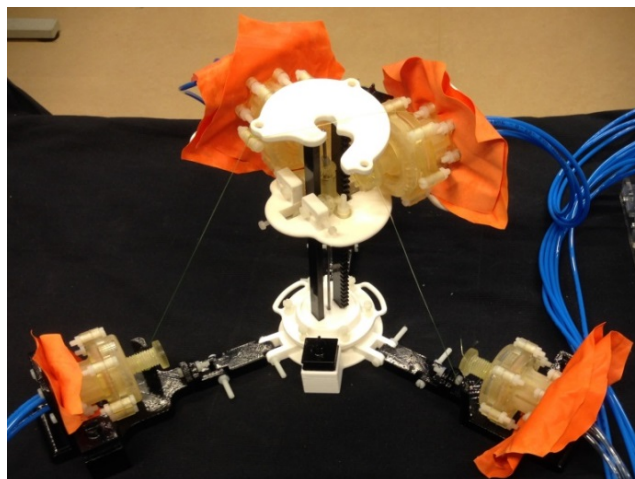
Figure 4. 2 Prototype of robot.

To activate the actuators, pneumatic valves, or a pneumatic valve terminal, are needed. The design of pneumatic valve is not included in this project. Therefore, the pneumatic distribution system shown in Figure 4.3, developed previously by Vincent Groenhuis, another student in RaM lab, is used to activate the actuators in McRobot. The detailed

---

[1] RaM: **R**obotics **a**nd **M**echatronics. A lab in the University of Twente, dealing with applications of modern systems and control methods to practical situations, focusing on robotics.

working principle of this pneumatic distribution system is represented in Vincent's master thesis.[47]

Figure 4. 3 The pneumatic distribution system.[47]

The overall system including the pneumatic distribution is shown in Figure 4.4.
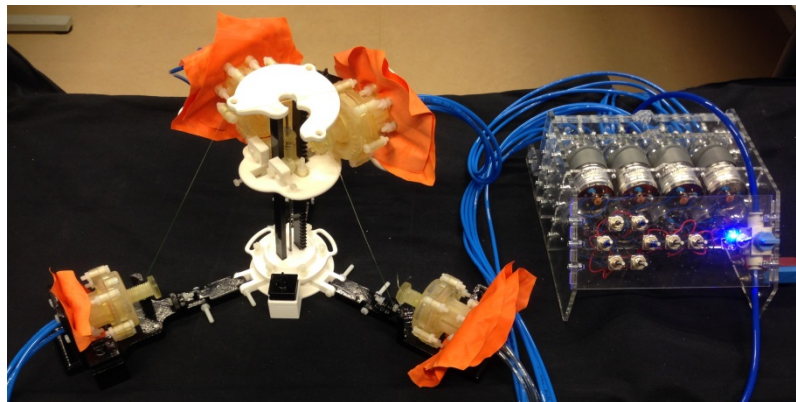
Figure 4. 4 Overall view of the prototype, including pneumatic distribution system.

The previously developed pneumatic distribution system contains eight DC motors, therefore activates eight actuators. In McRobot, only five actuators are needed, meaning that only five DC motors are connected with the robot through tubes.

4.2 Tests

The tests of McRobot, including the actuator, were conducted in both lab RaM and MRI scanner.

4.2.1 Tests in Lab

The actuator was tested with a dynamometer to measure the maximum output force in the rotational direction that the actuator can exert, as shown in Figure 4.5.
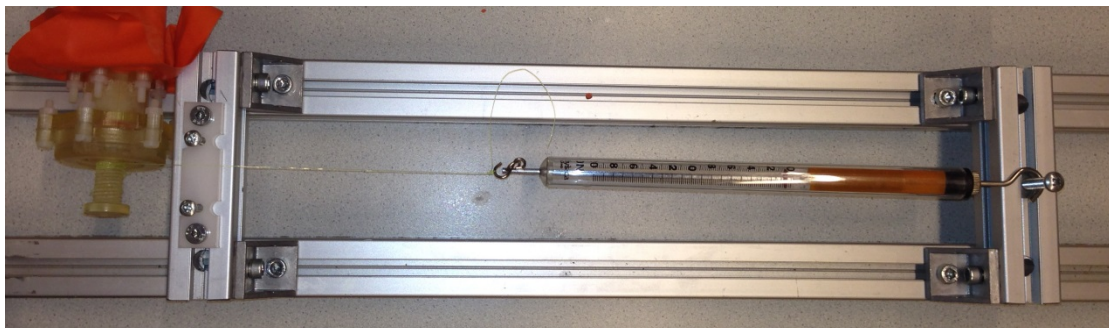
Figure 4. 5 Output force measurement instrument for actuator.

The test was performed at different air pressures. As the dynamometer is only a simple spring scale, it turned out to be not precise enough. Therefore the test was performed twice, with the first time the air pressure was decreased from 5bar to 2.5bar gradually and the second time increased from 2.5bar to 5bar. The actuator was operated until it failed. Then, the average between the two measurements was calculated. The measurement result is shown in Table 4.1 and Figure 4.6.

Table 4. 1 Output force measurement result of actuator.

Air Pressure (bar)	Decreased Pressure (N)	Increased Pressure (N)	Average Value (N)
5	19	21	20
4.5	15.2	14.8	15
4	13.5	13.6	13.55
3.5	12.2	12.8	12.5
3	10.4	10.8	10.6
2.5	5	5.6	5.3

Figure 4. 6 Output force measurement result of actuator.

As represented in previous chapter, the output torque of the actuator can be represented as:

$$F_T = \frac{T}{r_{avg}}$$

In which, T represents the output torque of the actuator, r_{avg} represents the average radius of output shaft, which can be assumed as r/2, where r represents the radius of rotor, which is 12.5mm.

Therefore the output torque of the actuator can be represented as:

$$T = F_T r_{avg} = \frac{F_T r}{2}$$

Therefore the output torque of the actuator, based on the measurement result of the output force, is shown in Table 4.2 and Figure 4.7.

Table 4. 2 Output torque of actuator.

Air Pressure (bar)	Decreased Pressure (Nmm)	Increased Pressure (Nmm)	Average Value (Nmm)
5	118.75	131.25	125
4.5	95	92.5	93.75
4	84.375	85	84.6875
3.5	76.25	80	78.125
3	65	67.5	66.25
2.5	31.25	35	33.125

Figure 4. 7 Output torque of actuator.

From the measurement result it can be seen that at the air pressure of 5bar the actual output torque is approximately 125Nmm, while the theoretical calculation is 50.02Nmm. This result indicates that the friction between the gears is overestimated and the safety factor of the project is approximately 2.5.

The step motion of the actuator is measured roughly to be 12°. With a lab-made DC motor based pneumatic distributor, a speed of approximately 1.25rad/s can be achieved. This speed is limited due to the limited rotation speed of motor. The speed can be increased by replacing the lab-made DC motor based pneumatic distributor with commercial valve terminal with higher frequency.

The insertion accuracy and maximum speed of the tool are measured roughly to be 2mm and 11.6mm/s respectively. Similar with that in actuator, by replacing the DC motor based pneumatic distributor with commercial valve terminal with higher frequency, the insertion speed can be increased as well.

4.2.2 Test in MRI Scanner

Before this functional prototype, a demonstrative model was 3D printed out of the same materials and tested inside an MRI scanner. The demonstrative model was attached on a human body and scanned inside the MRI scanner, as shown in Figure 4.8.

Figure 4. 8 Demonstrative model attached on a human body inside MRI scanner.

The obtained MRI image is shown in Figure 4.9.
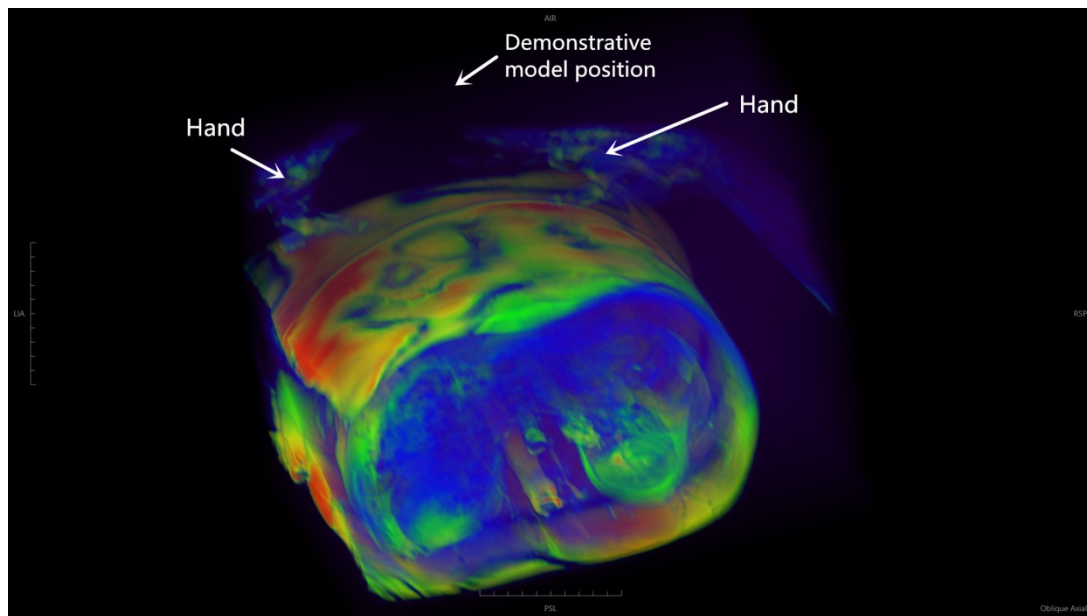
Figure 4. 9 MRI image of demonstrative model.

It can be seen from Figure 4.8 and Figure 4.9 that the demonstrative model is geometrically compatible with the MRI scanner. The model is invisible in the MRI image and no image artifacts introduced by the model was observed, indicating that the demonstrative model is fully MRI compatible. In Figure 4.9, the patient puts his hands on the model, indicating the position of the model, as the model is invisible in the image.

The functional prototype of McRobot (shown in Figure 4.2) was tested inside an MRI scanner as well, being fixed on a silicone gel based soft phantom, instead of human body. Both the demonstrative model and the functional prototype are made out of same materials and same dimension. Figure 4.10 is the MRI image of the functional prototype obtained from the scanner. The prototype is invisible in the image and no image artifacts introduced by the prototype was observed either, indicating that the prototype is indeed fully MRI compatible. As the functional prototype is of the same dimension with the demonstrative model, it is therefore geometrically compatible with the MRI scanner as well, although it was not tested on human body. One failed test was the control. The prototype was tried to penetrate the soft phantom inside the MRI scanner by the control of the pneumatic distribution system located outside the MRI room, through the connection of long air tubes. However, this test failed. Possible reasons are the air leakage in the distribution system and the air pressure drop during the long transmission.
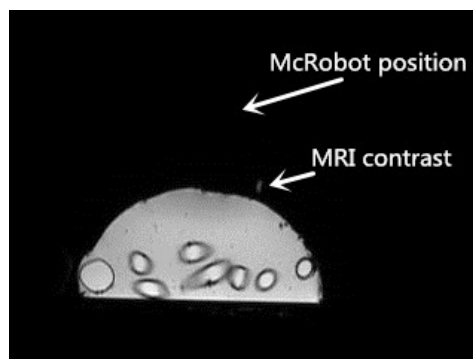
Figure 4. 10 MRI test result.

5. Conclusions and Future Works

Prior to this project, an initial concept of McRobot including four DoFs was designed. In this project, the concept is further designed in detail and a prototype is produced in the lab RaM by 3D printing and laser cutting equipment. This prototype proves the functions and the exposed problems during the tests are represented in this chapter as the guidance for future work.

5.1 Conclusions

The prototype of McRobot, including the actuators, can be made out of resin, ABS, and Delrin by 3D printing and laser cutting equipment.

The step motion, maximum speed, and output torque of the actuator are approximately 12°, 1.25rad/s, and 125Nmm respectively, which achieve the requirements. Both the speed and output torque can be increased by replacing a valve terminal with higher frequency and increasing the air pressure.

The robot provides an insertion accuracy and maximum insertion speed of approximately 2mm and 11.6mm/s respectively. The tool is able to penetrate a silicone gel based soft phantom. Therefore the insertion force is believed to be not smaller than 4N. As a DC motor based pneumatic distributor system is applied currently, the insertion speed can be therefore controlled by adjusting the motor rotation speed. When this distributor system is replaced by a commercial pneumatic valve terminal, the insertion speed can be controlled by adjusting the frequency of the valve terminal. The robot is MRI compatible and adapts the compact size between the patient and imager bore. Both active and passive operation modes can be achieved. In the passive mode, back-drivability can be achieved. A patient-mounted concept compensates the patient motion passively.

The pneumatic actuator designed in this project is similar with the one developed by Hiroyuki Sajima et al. mentioned in state of art.[16] Compared with the one developed by Hiroyuki Sajima et al., the new actuator designed in this project has some advantages. For instance, the new actuator is back-drivable and the friction inside the actuator is smaller due to the application of ball bearing. The actuator developed by Hiroyuki Sajima et al. does not contain a specialized return mechanism for the pistons. Therefore when returning, the rotation gear pushes the three direct acting gears back by force, which introduces energy waste and longer return time. The new designed actuator contains elastic material as a specialized return mechanism. With this return mechanism, the pistons return to zero position immediately after stroke, and the friction between the rotor and pistons is reduced.

5.2 Future Works

The design of the carriage needs to be improved. Currently, it introduces tilt and friction between the guidance and both of them need to be reduced as much as possible.

More measurements in MRI scanner are needed. The accuracy and speed of the tool is not yet measured in a real MRI scanner but only measured visually in lab. The speed of the actuator depends dominantly on the frequency of valves. Therefore, a commercial valve terminal with higher frequency will theoretically result in higher maximum speed, which is currently limited due to the DC motors. Other measurements, such as the insertion force and the torque of axial rotation of the tool, are needed as well.

Currently, the material working as the diaphragm is weak and it breaks in higher pressures, which results in the actuator unstable. Therefore a more suitable material needs to be found out.

The pneumatic distribution system couples every two tubes due to its 8-shape rubber ring, which means it is possible that sometime two tubes are compressed with air and therefore two pistons are pushed at the same time. And this system does contain any exhaust port, which results in that the piston cannot return to the zero position immediately due to that the air in the corresponding tube cannot be fast decompressed. What is more, the leakage of this system is obvious. Therefore a more suitable commercial pneumatic valve terminal which can be computer-controlled needs to be found out.

More precise kinematic and kinetic models for actuator and robot are needed. As for the actuator, in the force analysis model of the rotor and piston, the assumed values and the calculated values based on assumed ones, such as the friction between the teeth and the stiffness coefficient of return mechanisms, etc., need to be replaced by actual measurement result. The neglected factors, such as the friction coefficients of static friction and kinetic friction between the piston and cylinder and the viscosity coefficient of lubrication, need to be taken into consideration. And the neglected factors in the model of step motion need to be taken into consideration as well. What is more, a more precise finite element modelling (FEM) analysis of rotor and piston is needed in the future. As for the robot, the frictions between different elements and the weights of them, which are currently neglected, need to be taken into consideration. In the current kinematic model of robot, some distances are neglected: The center of motion is assumed to be located directly on the patient's skin, while in reality there is a distance between the center of motion and patient's skin. Although this distance should be as small as possible, it still cannot be totally removed. The three ropes connecting the baselegs and top plate are assumed to connect at a common point on top of the tool guide, while in reality they are connected on the top plate and the three connection points have distances between each other. In the more precise kinematic model, these neglected distances need to be taken into consideration.

Reference

[1]   J. Xu, K. D. Kochanek, and S. L. Murphy, "Deaths: Final Data for 2007," *Natl. Vital Stat. Reports*, vol. 58, no. 19, 2010.

[2]   D. L.Hoyert and J. Xu, "Deaths: preliminary data for 2011," *Natl. Vital Stat. Reports*, vol. 61, no. 6, 2012.

[3]   J. A. J. Graafmans, "Conceptual design and modeling of end-effector for McRobot," Eindhoven University of Technology, 2013.

[4]   N. V Tsekos, A. Khanicheh, E. Christoforou, and C. Mavroidis, "Magnetic Resonance-Compatible Robotic and Mechatronics Systems for Image-Guided Interventions and Rehabilitation: A Review Study," *Annu. Rev. Biomed. Eng.*, vol. 9, pp. 351–87, Jan. 2007.

[5]   N. Hata, R. Hashimoto, J. Tokuda, and S. Morikawa, "Needle Guiding Robot for MR-Guided Microwave Thermotherapy of Liver Tumor using Motorized Remote-Center-of-Motion Constraint," in *Proceedings of the 2005 IEEE International Conference on Robotics and Automation*, 2005, no. April, pp. 1652–1656.

[6]   N. V Tsekos, J. Shudy, E. Yacoub, P. V Tsekos, and I. G. Koutlas, "Development of a Robotic Device for MRI-Guided Interventions in the Breast."

[7]   B. T. Larson, E. Arthur G, N. V. Tsekos, E. Yacoub, P. V Tsekos, and I. G. Koutlas, "Design of an MRI-Compatible Robotic Stereotactic Device for Minimally Invasive Interventions in the Breast†," *J. Biomech. Eng.*, vol. 126, no. 4, pp. 458–465, Sep. 2004.

[8]   N. V. Tsekos, A. Özcan, and E. Christoforou, "A Prototype Manipulator for Magnetic Resonance-Guided Interventions Inside Standard Cylindrical Magnetic Resonance Imaging Scanners," *J. Biomech. Eng.*, vol. 127, no. 6, p. 972, 2005.

[9]   E. Christoforou, E. Akbudak, A. Ozcan, M. Karanikolas, and N. V Tsekos, "Performance of interventions with manipulator-driven real-time MR guidance: implementation and initial in vitro tests," *Magn. Reson. Imaging*, vol. 25, no. 1, pp. 69–77, Jan. 2007.

[10]   I. Bricault, N. Zemiti, E. Jouniaux, C. Fouard, E. Taillant, F. Dorandeu, and P. Cinquin, "A Light Puncture Robot for CT and MRI Interventions," *IEEE ENGINEERING IN MEDICINE AND BIOLOGY MAGAZINE*, no. June, pp. 42–50, 2008.

[11]   C. J. Walsh, N. C. Hanumara, A. H. Slocum, J.-A. Shepard, and R. Gupta, "A Patient-Mounted, Telerobotic Tool for CT-Guided Percutaneous Interventions," *J. Med. Device.*, vol. 2, no. 1, pp. 011007–1–011007–10, 2008.

[12]   B. Maurin, B. Bayle, O. Piccin, and J. Gangloff, "A Patient-Mounted Robotic Platform for CT-Scan Guided Procedures," *IEEE Trans. Biomed. Eng.*, vol. 55, no. 10, pp. 2417–2425, 2008.

[13]   A. Melzer, B. Gutmann, T. Remmele, R. Wolf, A. Lukoscheck, M. Bock, H. Bardenheuer, and H. Fischer, "INNOMOTION for Percutaneous Image-Guided Interventions," *IEEE ENGINEERING IN MEDICINE AND BIOLOGY MAGAZINE*, no. JUNE, pp. 66–73, 2008.

[14]   M. Bock, A. Melzer, H. Bardenheuer, H. Ghaderi, B. Gutmann, H. Zimmermann, and W. Semmler, "MR-guided percutaneous interventions using a robotic assistance system: initial experiences in a pig model," *Proc. Intl. Soc. Mag. Reson. Med.*, vol. 13, p. 2662, 2005.

[15]   K. Suzumori, T. Hashimoto, K. Uzuka, and I. Enomoto, "Pneumatic Direct-drive Stepping Motor for Robots," in *Proceedings of the 2002 IEEE/RSJ Intl. Conference on Intelligent Robots and Systems*, 2002, no. October, pp. 2031–2036.

[16]   H. Sajima, I. Sato, H. Yamashita, T. Dohi, and K. Masamune, "TWO-DOF NON-METAL MANIPULATOR WITH PNEUMATIC STEPPING ACTUATORS FOR NEEDLE PUNCTURING INSIDE OPEN-TYPE MRI," in *World Automation Congress*, 2010, no. 1, pp. 3–8.

[17]   D. Stoianovici, A. Patriciu, D. Petrisor, D. Mazilu, and L. Kavoussi, "A New Type of Motor: Pneumatic Step Motor," *IEEE/ASME Trans. MECHATRONICS*, vol. 12, no. 1, pp. 98–106, 2007.

[18]   B. Vigaru, D. Petrisor, A. Patriciu, D. Mazilu, and D. Stoianovici, "MR compatible actuation for medical instrumentation," in *2008 IEEE International Conference on Automation, Quality and Testing, Robotics*, 2008, pp. 49–52.

[19]   Y. Chen, K.-W. Kwok, and Z. T. H. Tse, "An MR-Conditional High-Torque Pneumatic Stepper Motor for MRI-Guided and Robot-Assisted Intervention," *Ann. Biomed. Eng.*, vol. 42, no. 9, pp. 1823–1833, Sep. 2014.

[20]   Y. Chen, C. D. Mershon, and Z. T. H. Tse, "A 10-mm MR-Conditional Unidirectional Pneumatic Stepper Motor," *IEEE/ASME Trans. MECHATRONICS*, vol. 20, no. 2, pp. 782–788, Apr. 2015.

[21]   H. Elhawary, Z. T. H. Tse, A. Hamed, M. Rea, B. L. Davies, and M. U. Lamperth, "The case for MR-compatible robotics: a review of the state of the art," *Int. J. Med. Robot. Comput. Assist. Surg.*, vol. 4, no. 2, pp. 105–113, Jun. 2008.

[22]   D. Stoianovici, "Multi-imager compatible actuation principles in surgical robotics," *Int. J. Med. Robot. Comput. Assist. Surg.*, vol. 01, no. 02, pp. 86–100, 2005.

[23]   J. F. Schenck, "The role of magnetic susceptibility in magnetic resonance imaging: MRI magnetic compatibility of the first and second kinds," *Int. J. Med. Phys. Res. Pract.*, vol. 23, no. 6, pp. 815–850, 1996.

[24]   R. Gassert, R. Moser, E. Burdet, and H. Bleuler, "MRI/fMRI-Compatible Robotic System with Force Feedback for Interaction with Human Motion," *IEEE/ASME Trans. MECHATRONICS*, vol. 11, no. 2, pp. 216–224, 2006.

[25]   R. Gassert, E. Burdet, and K. Chinzei, "Opportunities and Challenges in MR-Compatible Robotics: Reviewing the History, Mechatronic Components, and Future

Directions of this Technology," *IEEE ENGINEERING IN MEDICINE AND BIOLOGY MAGAZINE*, no. June, pp. 15–22, 2008.

[26]   R. Gassert, L. Dovat, O. Lambercy, Y. Ruffieux, D. Chapuis, G. Ganesh, E. Burdet, and H. Bleuler, "A 2-DOF fMRI Compatible Haptic Interface to Investigate the Neural Control of Arm Movements," in *Proceedings 2006 IEEE International Conference on Robotics and Automation, 2006. ICRA 2006.*, 2006, pp. 3825–3831.

[27]   R. C. Susil, A. Krieger, J. A. Derbyshire, A. Tanacs, L. L. Whitcomb, G. Fichtinger, and E. Atalar, "System for MR Image–guided Prostate Interventions: Canine Study," *Radiology*, vol. 228, no. 3, pp. 886–984, 2003.

[28]   M. F. Dempsey, B. Condon, and D. M. Hadley, "Investigation of the Factors Responsible for Burns During MRI," *J. Magn. Reson. IMAGING*, vol. 13, no. 4, pp. 627–631, Apr. 2001.

[29]   H. Elhawary, A. Zivanovic, M. Rea, B. L. Davies, C. Besant, D. M. C. Robbie, N. M. Desouza, I. Young, and M. U. Lamperth, "A Modular Approach to MRI-Compatible Robotics," *IEEE ENGINEERING IN MEDICINE AND BIOLOGY MAGAZINE*, vol. i, no. June, pp. 35–41, 2008.

[30]   Y. Koseki, T. Washio, K. Chinzei, and H. Iseki, "Endoscope Manipulator for Trans-nasal Neurosurgery, Optimized for and Compatible to Vertical Field Open MRI," in *5th International Conference on Medical Image Computing and Computer-Assisted Intervention*, 2002, pp. 114–121.

[31]   M. Tada, S. Sasaki, and T. Ogasawara, "Development of an Optical 2-axis Force Sensor Usable in MRI Environments," *Sensors, 2002. Proc. IEEE*, pp. 984–989.

[32]   M. Tada and T. Kanade, "Development of an MR-Compatible Optical Force Sensor," in *Proceedings of the 26th Annual International Conference of the IEEE Engineering in Medicine and Biology Society.*, 2004, vol. 3, pp. 2022–2025.

[33]   D. Chapuis, R. Gassert, L. Sache, E. Burdet, and H. Bleuler, "Design of a Simple MRI/fMRI Compatible Force/Torque Sensor," in *Proceedings of 2004 IEEE/RSJ International Conference on Intelligent Robots and Systems*, 2004, no. section II, pp. 2593–2599.

[34]   E. Hempel, H. Fischer, L. Gumb, T. Hohn, H. Krause, U. Voges, H. Breitwieser, B. Gutmann, and J. Durke, "An MRI-Compatible Surgical Robot for Precise Radiological Interventions," *Comput. Aided Surg.*, vol. 8, pp. 180–191, 2003.

[35]   K. Chinzei, N. Hata, F. A. Jolesz, and R. Kikinis, "MR Compatible Surgical Assist Robot: System Integration and Preliminary Feasibility Study," in *The International Conference on Medical Image Computing and Computer-Assisted Intervention*, 2000, no. February 2000, pp. 921–930.

[36]   K. Chinzei, R. Kikinis, and F. A. Jolesz, "MR Compatibility of Mechatronic Devices: Design Criteria," *Med. Image Comput. Comput. Interv.*, vol. 1679, pp. 1020–1031, 1999.

[37]   D. H. J. M. va. den Hoogen, "Conceptual Mechanism Design and Kinematic Analysis of an MRI Compatible Surgery Robot," Eindhoven University of Technology, 2013.

[38]   E. G. Christoforou, N. V. Tsekos, and A. Özcan, "Design and Testing of a Robotic System for MR Image-guided Interventions," *J. Intell. Robot. Syst.*, vol. 47, no. 2, pp. 175–196, Sep. 2006.

[39]   H. Su, M. Zervas, G. a. Cole, C. Furlong, and G. S. Fischer, "Real-time MRI-Guided Needle Placement Robot with Integrated Fiber Optic Force Sensing," in *2011 IEEE International Conference on Robotics and Automation*, 2011, pp. 1583–1588.

[40]   M. van den Bosch, "MRI-guided robot for needle interventions in the prostate," Utrecht University, 2011.

[41]   C. J. Walsh, "Image-Guided Robots for Dot-Matrix Tumor Ablation," Massachusetts Institute of Technology, 2010.

[42]   N. Yu and R. Riener, "Review on MR-Compatible Robotic Systems," in *The First IEEE/RAS-EMBS International Conference on Biomedical Robotics and Biomechatronics*, 2006, pp. 661–665.

[43]   Invivo, *INTERVENTIONAL MRI: SOFT TISSUE, ORTHOPEDICS, NEURO*. 2005, pp. 1–23.

[44]   A. M. Okamura, C. Simone, and M. D. O'Leary, "Force Modeling for Needle Insertion Into Soft Tissue," *IEEE Trans. Biomed. Eng.*, vol. 51, no. 10, pp. 1707–1716, Oct. 2004.

[45]   P. Cinquin, A. Jacquet, and E. Taillant, "SYSTEM FOR POSITIONING AN OBSERVATION AND/OR INTERVENTION DEVICE ON A PATIENT," US 2006/0058640 A1, 2006.

[46]   H. H. Chen and B. S, "Quality Assessment of high spatial resolution for MRI."

[47]   V. Groenhuis, "Improving Accuracy and Efficiency in MRI-navigated Breast Biopsy," University of Twente, 2014.

Appendices

A. Design of a Back-drivable Pneumatic Step Actuator

The design of pneumatic actuator is picked up as an individual paper as following:

Design of a Back-drivable Pneumatic Step Actuator

Abstract

Magnetic resonance imaging (MRI) compatible robotics is one of the new technologies for performing image guided minimally invasive interventions (MII) such as cancer biopsy gathering or brachytherapy. In this paper, the design of an MRI compatible back-drivable pneumatic step actuator is reported. This actuator achieves a step motion of 12°. The speed of the actuator depends on the frequency of the valves. With a lab-made DC motor based pneumatic distributor, a speed of 1.25rad/s can be achieved. By replacing the distributor with a commercial pneumatic valve terminal with higher frequency, the speed can be increased. With the air pressure of 5bar, an output torque of 125Nmm can be achieved. Test inside the MRI scanner indicates that this actuator is fully MRI compatible. The actuator is installed into an MRI compatible surgical robot consisting of four degrees of freedom (DoF), indicating its potential application.

Key Words: MRI compatible, back-drivable, pneumatic step actuator

1. Introduction

Cancer was the second-leading cause of death worldwide.[1][2] New technologies preventing and solving cancer are therefore developed. Minimally invasive surgery (MIS) is one of these technologies. MIS does not invade patient by large incisions, therefore resulting in a quicker recovery time and less infection possibility.[3] In the process of MIS, in order to guide the tool to the desired location, visual feedback is required. Magnetic resonance imaging (MRI) is an attractive method offering the visual feedback due to its advantages. Firstly, MRI offers a plethora of soft-tissue contrast mechanisms. Secondly, MRI is an intrinsically 3D modality that allows unrestricted selection of oblique 3D or multi-plane imaging. Thirdly, MRI does not use ionizing radiation therefore is safe for the patient.[4] Robotics is another promising development of the new technologies. Robotics offer higher accuracy, efficiency, and steadiness level than manual operations. The combination of MIS, MRI and robotics, which is the MRI compatible assistant robot for minimally invasive interventions, is believed to be an ideal method of cancer diagnosis and treatment.

Many groups around the world have reported different designs of MRI compatible robots for minimally invasive interventions (MII) in last decades.[5][6][7][8][9][10][13][14] Few clinical available products, however, have been published due to various difficulties. One important part of a robot is the actuator. To actuate the MRI compatible robots, traditional electromagnetic actuators, piezoelectric actuators and pneumatic actuators are three main strategies. However, neither electromagnetic actuators nor piezoelectric actuators can operate inside the MRI scanner. Therefore, many groups have been focused on the design of pneumatic actuators.[15][16][17][18][19][20]

In this paper, a new designed back-drivable pneumatic step actuator is represented. The components of this actuator are made out of MRI compatible materials. The actuator is installed into a four-degrees-of-freedom (DoF) MRI compatible surgical robot showing its potential application. The test inside an MRI scanner indicates that the actuator is fully MRI compatible.

2. Conceptual Design

2.1 Working Principle

A 2D schematic diagram indicating the working principle of this pneumatic step actuator is shown in Figure 1. The working process of this actuator can be explained as: First, position 1 is pushed by high pressure air. Consequently the rotor rotates and meshes with piston 1. Then, piston 2 is pushed and the rotor rotates one more step. At the same time, piston 1 is pushed back by a return mechanism. Similarly, piston 3 is pushed and the rotor rotates one step further, meanwhile, piston 2 is pushed back. The repetition of this operation keeps the rotor rotating continuously. Switching the pushing sequence of pistons can switch the rotation direction.
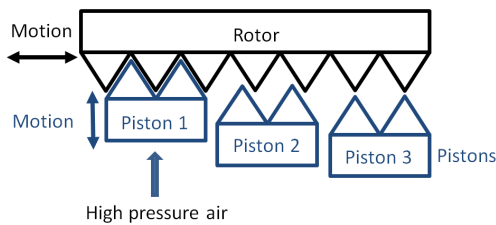
Figure 1 Principle representation of the pneumatic step actuator.

To return the piston to its zero position after meshing and reduce the number of required hoses, flexible material, such as a rubber bar, is used as the return mechanism, working as a spring, to push back the pistons.

2.2 Actuator Concept

As the actuator is desired to be used in an MRI environment, it therefore must be MRI safe and MRI compatible. For functional expectation, the actuator should be back-drivable and the friction inside the actuator should be as small as possible.

The step rotational motion is realized by two types of gears, which are rotor and pistons. To guarantee that the gears mesh perfectly, the teeth on both rotor and pistons have the same sizes. The main components of the actuator and their arrangement are shown in Figure 2.
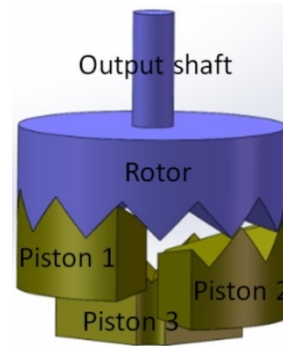
Figure 2 Main components of the actuator.

3. Theoretical Analysis

3.1 Rotor Size

The precision of the actuator can be achieved by designing the size of rotor. The arc length of the rotor corresponding to the step motion is represented as:

$$\delta L = \frac{d \delta \theta}{2}$$

In which, δL represents the arc length of the rotor corresponding to a step motion, which is one third length of the tooth pitch, as shown in Figure 3. d represents the diameter of the rotor. $\delta \theta$ represents the step motion of the actuator.
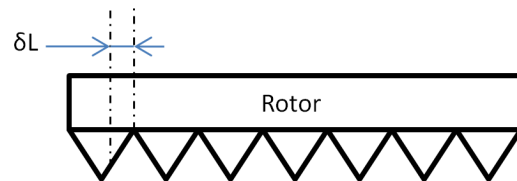
Figure 3 Arc length δL corresponding to a step motion.

3.2 Force Analysis

The force analysis model of the rotor and piston is shown in Figure 4.
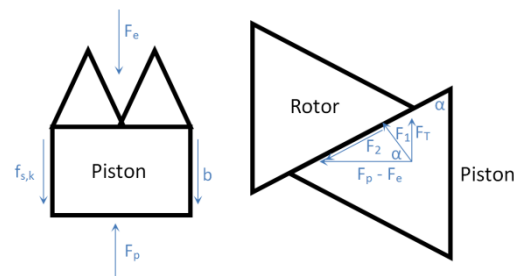
Figure 4 Force analysis of rotor and piston.

In which, $f_{s,k}$ represent the friction coefficients of static friction and kinetic friction between the piston and cylinder. b represents the viscosity coefficient when lubrication is applied. F_p represents the

thrust force received by the piston from the high pressure air. F_e represents the elastic force generated by the flexible material when being compressed as a return mechanism. As the friction between the piston and cylinder is small compared to the thrust force and elastic force, and no lubrication is applied currently, both $f_{s,k}$ and b are therefore neglected to simplify the calculation. F_1 and F_2 represent the component force of the interaction force between two teeth, which is F_p-F_e, in the orthogonal directions. F_T represents the tangential force received by the rotor that rotates the rotor around its axis. α represents the base angle of tooth.

The piston received force F_p from high pressure air can be represented as:

$$F_p = Ap$$

In which, A represents the cross-sectional area of piston. p represents the air pressure of high pressure air.

The relation between the actuator output torque T and force in the tangential direction F_T, received by the rotor, can be represented as:

$$F_T = \frac{T}{r_{avg}}$$

In which, r_{avg} represents the average radius of output shaft, which can be assumed as r/2, where r represents the radius of rotor.

From the force analysis in Figure 4, to overcome the friction and achieve effective motions of rotor and piston, the shearing force on the tooth surface should be no less than the friction between the tooth surfaces:

$$F_2 = \mu F_1$$

In which, μ represents the friction coefficient between the tooth surfaces of rotor and piston.

From the force analysis of piston and rotor separately, the following equation and inequation can be obtained:

$$F_p - F_e = F_1 \cos\alpha + F_2 \sin\alpha$$

$$F_T \le F_1 \sin\alpha - F_2 \cos\alpha$$

Equality holds when the acceleration of the piston is neglectable.

To avoid the self-lock, the following condition needs to be satisfied:

$$(F_p - F_e)\sin\alpha > \mu(F_p - F_e)\cos\alpha$$

It is possible to reduce the air pressure and increase the cross-sectional area of piston to obtain the same F_p, consequently the same output torque. However, considering the compact area available for the actuator, to increase the air pressure but limit the dimension of piston is preferred.

The stiffness coefficient k_e of the flexible material can be represented as:

$$k_e = \frac{F_e}{\Delta x}$$

In which, Δx represents the stroke of a piston.

The Young's modulus E of the flexible material can be represented as:

$$E = \frac{k_e L_0}{A_0}$$

In which, L_0 and A_0 represent the original length and original cross-sectional area of the flexible respectively.

3.3 Valve Frequency

Three pistons are required to activate the actuator. Therefore three pneumatic valves, or a valve terminal with at least three outputs, are required to pressurize and decompress the cylinder of the actuator. The inputs of the valves are connected with the high pressure air source and the outputs are connected with the cylinders respectively. The outputs pressurize and decompress the cylinders in sequence in order to drive the actuator correctly.

The model of a single step motion of the actuator can be represented as Figure 5.
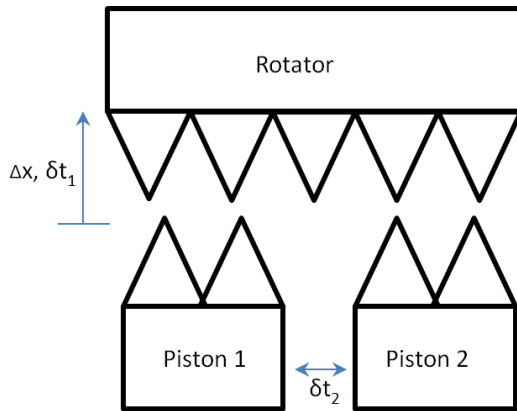
Figure 5 model of two adjacent pistons in cooperation with a rotor.

Δx represents the stroke of a single piston. δt_1 represents the duration for a single piston to operate from its zero position to end position and then be pushed back to the zero position by the return mechanism. δt_2 represents the interval between the operations of two adjacent pistons.

The duration, δt, which is consumed to achieve a completed step motion, can be represented as:

$$\delta t > \delta t_1$$

The output speed of the actuator can be represented as:

$$\omega = \frac{\delta\theta}{\delta t} = \frac{\delta\theta}{\delta t_2}$$

The frequency f of the operation of pistons can be represented as:

$$f = \frac{1}{\delta t} = \frac{\omega}{\delta\theta}$$

The frequency of the pneumatic valve terminal cannot be too high, because the piston needs time to return to its zero position before the next positon to be activated. When selecting the pneumatic valve terminal, the frequency of the terminal should be no larger than f.

4. CAD Model

The assembly, exploded view, and cross section of the actuator are shown in Figure 6-Figure 8.
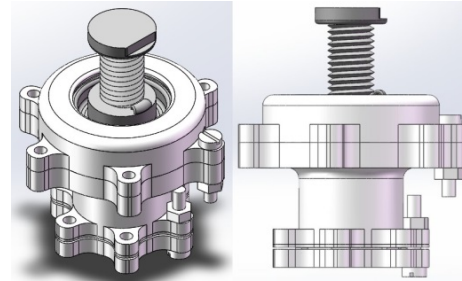
Figure 6 Assembly of the actuator.

Flexible material (Rubber bar)

Diaphragm (Rubber membrane)
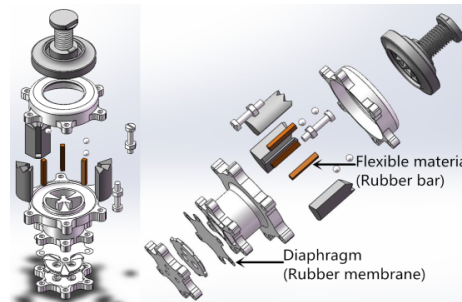
Figure 7e Exploded view of the actuator.
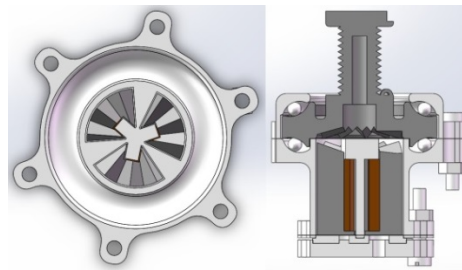
Figure 8 Top and side cross section of the actuator.

Plastic balls are distributed above and underneath the rotor, working as a ball bearing, to reduce the fiction. The return mechanism, which consists of three rubber bars, is integrated inside the actuator so that the design is more. The stroke of pistons is longer than the tooth depth of rotor and pistons so that the rotor does not contact the pistons which are in zero position, guaranteeing smooth rotation. A rubber membrane is fixed on the underneath of cylinders, working as a diaphragm, to avoid the air leakage from air tubes to the cylinders.

5. Prototype and Experiment

5.1 Prototype

A prototype of the pneumatic actuator is shown in Figure 9. The main components, the rotor and pistons, as well as the cylinder and head cover, are 3D printed out of resin. The screws, nuts are made out of nylon. The shims, which are used to control the friction

in the ball bearing, are laser cut out of polyester. The diaphragm is cut out of latex.
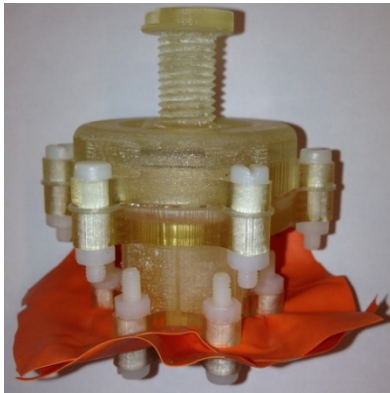
Figure 9 Prototype of the pneumatic actuator.

5.2 Experiment

The actuator was tested with a dynamometer to measure the maximum output tangential force that the actuator can exert, as shown in Figure 10.

Figure 10 Output force measurement instrument for actuator.

The test was conducted at different air pressures. As the dynamometer is only a simple spring scale, it turned out to be not precise enough. Therefore the test was conducted twice, with the first time the air pressure was decreased from 5bar to 2.5bar gradually and the second time increased from 2.5bar to 5bar. The actuator was operated until it failed. Then, the average data between the two measurements was calculated. The measurement result is shown in Table 1 and Figure 11.

Table 1 Output force measurement result of actuator.

Air Pressure (bar)	Decreased Pressure (N)	Increased Pressure (N)	Average Value (N)
5	19	21	20
4.5	15.2	14.8	15
4	13.5	13.6	13.55
3.5	12.2	12.8	12.5
3	10.4	10.8	10.6
2.5	5	5.6	5.3

Figure 11 Output force of the actuator (average).

The output torque of the actuator can be obtained based on the measured force, as shown in Table 2 and Figure 12.

Table 2 Output torque of actuator.

Air Pressure (bar)	Decreased Pressure (Nmm)	Increased Pressure (Nmm)	Average Value (Nmm)
5	118.75	131.25	125
4.5	95	92.5	93.75
4	84.375	85	84.6875
3.5	76.25	80	78.125
3	65	67.5	66.25
2.5	31.25	35	33.125

Figure 12 Output torque of the actuator (average).

The step motion of the actuator was roughly measured to be 12°. The rotation speed was measured with the drive of a lab-made DC motor based pneumatic distributor. With the limited rotation speed of DC motor, a maximum speed of the actuator was achieved to be approximately 1.25rad/s. It is believed that with a commercial pneumatic valve terminal with higher frequency, higher speed can be obtained.

6. Applying to McRobot

The designed actuators are applied to actuate an **M**RI **c**ompatible **Robot** (McRobot), which is shown in Figure 13.
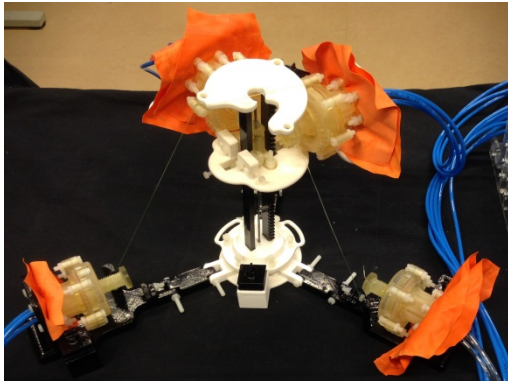
Figure 13 Prototype of McRobot with application of pneumatic step actuator.

The robot is consisted of four DoFs, which are two orientation DoFs, one insertion DoF, and one rotation DoF for the puncture needle around its axis. Five actuators are used to actuate the four DoFs. With the lab-made DC motor based pneumatic distributor, the robot works effectively to control all the four DoFs.

Insertion accuracy and speed of 2mm and 11.6mm/s respectively were achieved by the robot. With the new designed actuators, the robot penetrated its tool to a silicone gel based soft phantom successfully.

The robot, including the actuators, was tested inside an MRI scanner fixed on the soft phantom. The robot is invisible in the MRI image and no image artifacts introduced by the robot was observed, indicating that the robot, including the

actuators, is fully MRI compatible. The test image is shown in Figure 14.
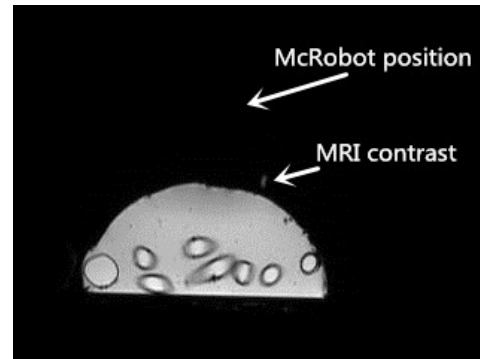
Figure 14 MRI test result.

7. Conclusions

A new type of MRI compatible pneumatic back-drivable step actuator was designed. The potential of the actuator was approved by applying it to an MRI compatible surgical robot.

The step motion of the actuator is 12°. With a lab-made DC motor based pneumatic distributor, a speed of 1.25rad/s can be achieved. With the air pressure of 5bar, an output torque of 125Nmm can be achieved. The speed can be increased by replacing the lab-made DC motor based pneumatic distributor with commercial valve terminal with higher frequency. The output torque can be increased by increasing the air pressure.

Reference

The reference of this individual paper is integrated into the reference of the report.

B. Matlab Codes

The codes compiled in Matlab for the test analysis of the actuator are shown as following:

```matlab
%% Force vs. Pressure Measurement
% All data
x_de=[5 4.5 4 3.5 3 2.5];   % Pressure decreased
x_in=[2.5 3 3.5 4 4.5 5];   % Pressure increased

y_de=[19 15.2 13.5 12.2 10.4 5];   % Date measured with decreased
pressure
y_in=[5.6 10.8 12.8 13.6 14.8 21];  % Date measured with increased
pressure

figure
hold on
plot(x_de,y_de,'r-s','MarkerFaceColor','r')
plot(x_in,y_in,'b-^','MarkerFaceColor','b')
legend('Decreased Air Pressure','Increased Air
Pressure','location','SouthEast')
hold off
grid on
xlabel('Air Pressure (bar)');
ylabel('Output Force (N)');
set(gca,'xtick',(2:0.5:5.5),'ytick',(4:2:22),'GridLineStyle','--
','box','on')
axis([2,5.5,4,22])
title({('Actuator Output Performance');('Output Force vs. Air
Pressure')});

%% Force vs. Pressure Measurement
% Average data
y_de_ave=(y_de+fliplr(y_in))/2;    % Average result between two
measurements

figure
plot(x_de,y_de_ave,'g-d','MarkerFaceColor','g')
legend('Average Test Result','location','SouthEast')
grid on
xlabel('Air Pressure (bar)');
ylabel('Output Force (N)');
set(gca,'xtick',(2:0.5:5.5),'ytick',(4:2:22),'GridLineStyle','--
','box','on')
axis([2,5.5,4,22])
title({('Actuator Output Performance');('Output Force vs. Air
Pressure')});

%% Torque vs. Pressure Calculation
% All calculation
ytor_de=y_de*(12.5/2);   % Torque calculation with decreased
pressure
ytor_in=y_in*(12.5/2);   % Torque calculation with increased
pressure
                         % 12.5 is the average radius of rotor
figure
hold on
plot(x_de,ytor_de,'r-s','MarkerFaceColor','r')
plot(x_in,ytor_in,'b-^','MarkerFaceColor','b')
legend('Decreased Air Pressure','Increased Air
Pressure','location','SouthEast')
```

```matlab
hold off
grid on
xlabel('Air Pressure (bar)');
ylabel('Output Torque (Nmm)');
set(gca,'xtick',(2:0.5:5.5),'ytick',(25:10:140),'GridLineStyle','--
','box','on')
axis([2,5.5,25,140])
title({('Actuator Output Performance');('Output Torque vs. Air
Pressure')});

%% Torque vs. Pressure Calculation
% All Average calculation
ytor_de_ave=(ytor_de+fliplr(ytor_in))/2;    % Average result between
two calculations

figure
plot(x_de,ytor_de_ave,'g-d','MarkerFaceColor','g')
legend('Average Test Result','location','SouthEast')
grid on
xlabel('Air Pressure (bar)');
ylabel('Output Torque (Nmm)');
set(gca,'xtick',(2:0.5:5.5),'ytick',(25:10:140),'GridLineStyle','--
','box','on')
axis([2,5.5,25,140])
title({('Actuator Output Performance');('Output Torque vs. Air
Pressure')});
```